Int J Mater Form (2017) 10:139–171
DOI 10.1007/s12289-015-1262-7

REVIEW

Models for ductile damage and fracture prediction in cold bulk metal forming processes: a review

Trong Son Cao[1,2]

Received: 16 October 2014 / Accepted: 13 August 2015 / Published online: 8 September 2015
© Springer-Verlag France 2015

Abstract Ductile damage and fracture prediction in real size structures subjected to complex loading conditions has been of utmost interest in the scientific and engineering community in the past century. Numerical simulations with nonlinear finite element (FE) codes allow investigating various complicated problems for damage and fracture prediction in real scale models, which is an important topic in many industries, including metal forming industry. For all industrial cold forming processes, the ability of numerical modeling to predict ductile fracture is crucial. However, this ability is still limited because of the complex loading paths (multi-axial and non-proportional loadings) and important shear effects in several forming processes. The development robust damage and fracture prediction models is essential to obtain realistic results for both geometry precision and mechanical properties. The present article reviews the models in three approaches of ductile damage, namely: uncoupled phenomenological model (or fracture criteria), coupled phenomenological models, and micromechanics-based models, which have been developed to predict ductile fracture in metal forming processes. The objective is to supply to engineers and scientists an overview on a "top-down" procedure to be able to construct predictive tools for metal forming processes.

✉ Trong Son Cao
trong-son.cao@mines-paristech.fr
trongson.cao@arcelormittal.com

[1] Mines ParisTech, Center for Material Forming, UMR CNRS 7635, 06904, Sophia-Antipolis, France

[2] Present address: Maizières Proces, Voie Romaine, ArcelorMittal, Global Research and Development, BP 30320, 57283, Maizières-lès-Metz Cedex, France

Keywords Metal forming · Ductile damage · Fracture prediction · FE modeling · Mechanical tests

Introduction

In the modern world, products should be produced under low cost and severe environmental constraints, there is thus no longer place for the classical trial and error tests. With the increasing of computer power, numerical simulations with non-linear finite element (FE) codes allow investigating various complicated problems for damage and fracture prediction in recent decades. For all industrial cold forming processes, the ability of numerical modeling to predict ductile fracture is crucial. The common issue is to predict ductile damage and fracture in multi-axial and non-proportional loadings involving very large plastic strain, in which the damage may localize away from the maximum critical strain locations. Moreover, the shear effects in several processes are important, damage models thus must be able to capture the associated shear damage mechanism. There is thus real need to develop robust damage models for industrial applications. By "robustness", the challenges for a good model are three-fold: (1) physical mechanisms of the onset of damage and fracture must be captured; (2) the models have to be suitable for numerical implementation and must be "simple" enough for real-scale structure simulations; and (3) models parameters should be convenient for identification for massive applications. Solving these problems is the driving force of various studies since the last decades. While the detailed reviews on porous plasticity framework and continuum models were given in the literature Tvergaard [1], Benzerga and Leblond [2], and Besson [3], the present review focuses on practical considerations and the comparison between these two approaches and the uncoupled approach

(which is often preferred in industrial applications). It aims at summarizing different approaches of ductile damage and their applications to forming processes, with special attentions paid on models construction and calibration as well as their practical applications. The objective is to supply a full procedure to follow in order to obtain most reliable predictive results of ductile fracture for metal forming applications. The paper is organized as follows. Section "Ductile damage mechanisms" summarizes the mechanisms of ductile damage, followed by a review of damage models in three approaches, reported in Section "Reviews on damage models". Section "Experiments and models calibration" discusses experimental techniques used for model calibration. Section "Numerical modeling of crack growth" shows the application of damage models in predicting crack growths. Section "Fracture prediction in forming processes" summarizes applications to forming processes with several illustrations for bulk forming processes. Section "Discussions" provides the discussions on several important points that would be improved.

Ductile damage mechanisms

Introduction

Ductility is understood as an intrinsic ability of materials to undergo a certain amount of plastic deformation without fracture (or without *mesocrack* formation). The fracture of ductile metals occurs after microvoids or shear bands develop in the metal matrix, around inclusions or other discontinuities such as grain boundaries. The damage occurring under large plastic strain is called ductile damage (in opposition to brittle damage), and is frequently observed in metal forming failure. Microscopically, ductile damage is associated with voids nucleation, growth and coalescence under high and moderate stress triaxiality (i.e., the ratio between the mean stress to the von Mises equivalent stress), or shear band formation under low stress triaxiality. Macroscopically, ductile damage is represented as the progressive degradation of a material, which exhibits a decrease in material stiffness and strength. One of pioneers who analyzed the evolution of an isolated cylindrical void in a ductile elastoplastic matrix to reveal the role of microvoids in ductile failure was McClintock et al. [4]. McClintock [5], from an available solution for the deformation of elliptical holes in a viscous material, proposed a fracture criterion by the growth and coalescence of preexisting cylindrical holes in plastic materials. Rice and Tracey [6] studied the evolution of spherical voids in an elastic-perfectly plastic matrix. In these studies, the interaction between microvoids, the coalescence process and the hardening effects were neglected and failure was assumed to occur when the cavity radius would reach a critical value specific for each material. These results showed that void growth is governed by stress triaxiality through a very strong inverse dependence. Gurson [7], based on the work of [6], in an *upper bound analysis*[1] of a finite sphere containing an isolated spherical void in a rigid perfectly plastic matrix, employed the void volume fraction f (or porosity) as an internal variable to represent damage and its softening effect on material. The Gurson model, consisting of a plastically compressible yield locus, with the evolution laws for the internal state variables, represents a constitutive model for porous materials. It should be noted that, in this model, spherical voids are assumed to remain spherical. This assumption is only valid for purely hydrostatic stress state, but deficient when general three-dimensional stress states are involved, especially for shear dominated states, where significant void shape change can be observed. Further extensions of Gurson's framework were devoted to different aspects: prediction accuracy [8], void nucleation [9, 10], void coalescence [11–18], void shape effect (e.g., [15, 19]), void size effect (e.g., [20, 21]), void/particle interaction (e.g., [22]), void rotation in plane strain [17], isotropic strain hardening [23], kinematic hardening (e.g., [23–25]), plastic anisotropy (e.g., [26–28]), rate dependency (e.g., [1]), "shear" effect (e.g., [29, 30]).

Characterization of stress states

For an isotropic material, the stress state is characterized by the symmetric stress tensor (6 components) or its eigenvalues (3 principal stresses: $\sigma_1, \sigma_2, \sigma_3$). Material models can also be formulated in terms of the first stress invariant (I_1) together with the second and the third deviatoric stress invariants (J_2, J_3):

$$\begin{aligned} p &= -\sigma_m = -\frac{1}{3}\text{trace}(\boldsymbol{\sigma}) = -\frac{1}{3}(\sigma_1+\sigma_2+\sigma_3) \\ &= -\frac{I_1}{3} \end{aligned} \tag{1}$$

$$\begin{aligned} q &= \overline{\sigma} = \sqrt{\frac{3}{2}\boldsymbol{s}:\boldsymbol{s}} \\ &= \sqrt{\frac{1}{2}\left[(\sigma_1-\sigma_2)^2+(\sigma_2-\sigma_3)^2+(\sigma_3-\sigma_1)^2\right]} \\ &= \sqrt{3J_2} \end{aligned} \tag{2}$$

$$\begin{aligned} r &= \left(\frac{27}{2}\det(\boldsymbol{s})\right)^{1/3} \\ &= \left(\frac{27}{2}(\sigma_1-\sigma_m)(\sigma_2-\sigma_m)(\sigma_3-\sigma_m)\right)^{1/3} \\ &= \left(\frac{27}{2}J_3\right)^{1/3} \end{aligned} \tag{3}$$

[1] The upper bound method consists of two stages: (1) find a kinematically admissible velocity field (or a family of velocity fields that is compatible with the boundary conditions); (2) within the proposed family, find the one that minimizes the plastic dissipation.

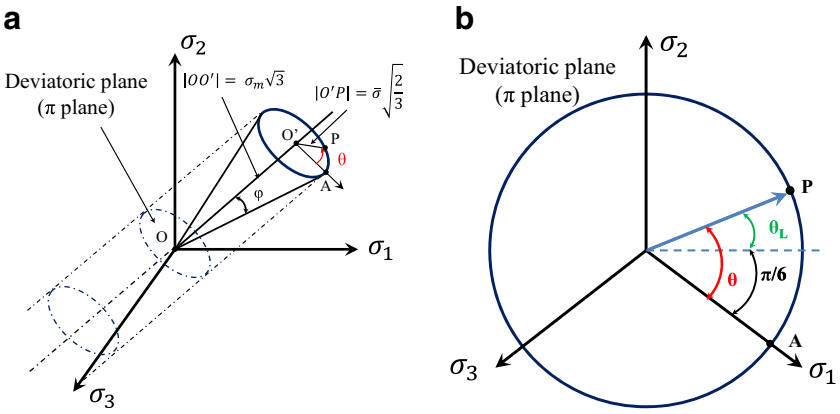

Fig. 1 Representation of the Lode angle **a** in the stress space; and **b** on the deviatoric plane

where p is the hydrostatic pressure; σ_m is the mean stress; q and r are two stress state parameters. In the ductile fracture community, the dimensionless hydrostatic pressure or the stress triaxiality ratio ($\eta = \frac{\sigma_m}{\bar{\sigma}}$) and the Lode angle θ are often used. The latter parameter is defined through the normalized third stress invariant:

$$\xi = \left(\frac{r}{q}\right)^3 = \cos(3\theta) \tag{4}$$

The geometrical representation of Lode angle θ is shown in Fig. 1a and b ($0 < \theta < \frac{\pi}{3}$ - for each sextant of the octahedral plane, the azimuth angle θ and the value of $\frac{27}{2}\frac{J_3}{\bar{\sigma}^3}$ can be one-to-one mapped).

A stress state can therefore be expressed in the spherical coordinate system of $(\overline{\sigma}, \eta, \theta)$ (see Fig. 1a [31]). The φ angle in Fig. 1a is related to the stress triaxiality by:

$$\eta = \frac{\sqrt{2}}{3}\tan^{-1}(\varphi) \tag{5}$$

The normalized Lode angle $\overline{\theta}$ is defined as:

$$\overline{\theta} = 1 - \frac{6\theta}{\pi} = 1 - \frac{2}{\pi}\arccos\left(\left(\frac{r}{q}\right)^3\right) \tag{6}$$

where r and q are defined in Eqs. 2 and 3, and the parameter $\overline{\theta}$ ($-1 \leq \overline{\theta} \leq 1$) will be called the Lode angle parameter hereinafter (or the Lode parameter). Some authors used another formula to calculate the Lode angle θ_L (e.g., [32]) and the Lode parameter μ or L (e.g., [33]):

$$\theta_L = \tan^{-1}\left(\frac{1}{\sqrt{3}}\frac{2\sigma_2 - \sigma_1 - \sigma_3}{\sigma_1 - \sigma_3}\right),$$
$$L = \mu = \frac{2\sigma_2 - \sigma_1 - \sigma_3}{\sigma_1 - \sigma_3} \tag{7}$$

where $-\frac{\pi}{6} < \theta_L < \frac{\pi}{6}$. These definitions and the definitions in Eqs. 4 and 6 are totally equivalent, which are linked by the following relation: $\theta_L = \theta - \frac{\pi}{6}$, $L = \mu \approx -\overline{\theta}$. The influence of the stress triaxiality and the Lode parameter (L) on the strain to localization (E_c) is illustrated in Fig. 2a and b obtaining from cell computations on an X100 steel (see Section "Cell computations").

As can be observed from these two figures (see also the results of [34–36]), the strain to localization decreases when the stress triaxiality increases (as pointed out by many authors in the literature, e.g., [5–7]) and the influence of

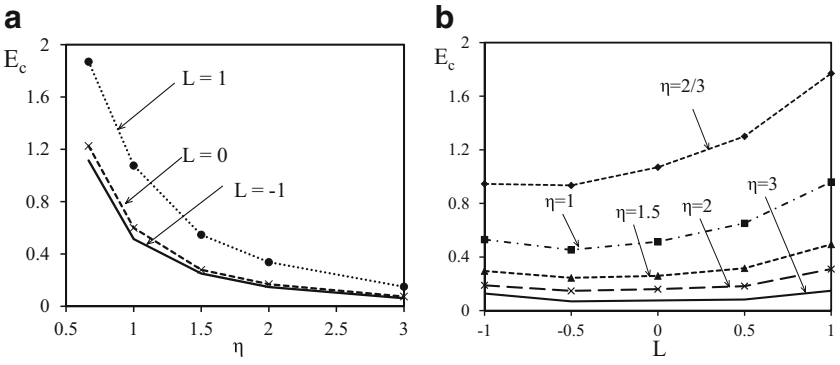

Fig. 2 Influence of **a** stress triaxiality, and **b** Lode parameter L on the localization strain for an X100 steel

the Lode parameter on the strain to localization is non-symmetric. In addition, both influences are more noticeable at low stress triaxiality [2].

Mechanisms dominating at positive stress triaxiality

In the high stress triaxiality regime, damage is governed by void nucleation, growth and coalescence (or linkage) mechanisms (in an elastoplastic/elastic matrix), which have been extensively studied in the literature.

Void nucleation

Unlike void growth (see Section "Void growth"), which would be treated independently of material hardening, the void nucleation process is strongly material-dependent. Generally, it depends on the particle strength, size and shape, as well as hardening of matrix material. Voids can be nucleated either by matrix-particle decohesion or by particle cracking. The decohesion mode of nucleation is favored in the case of soft matrices while the particle cracking mode is often observed in hard matrices [2]. Voids nucleate preferentially at large particles due to a higher probability of defects and local stress fields generated when the matrix undergoes plastic deformation. However, the voids created during this stage are small so they still do not have a visible influence on the material macroscopic behavior.

One of the pioneers of void nucleation modeling was Gurland and Plateau [37], who employed a energetic method (which was formulated from the balance of stored elastic strain energy and crack surface energy), to study the void nucleation due to the cracking of spherical particle. Goods and Brown [38] proposed another energy criterion to describe the nucleation by matrix-particle decohesion. Other criteria are often based on critical stress; some of them are listed below:

- Argon and Im [39] proposed a phenomenological critical stress condition based on a continuum plasticity approach:

$$\sigma_I^{\max} + \Sigma_h = \min(\sigma_c^I, \sigma_c^P) \tag{8}$$

  where $\sigma_I^{\max}$ is the maximum principal stress (local); Σ_h is the hydrostatic stress (remote); σ_c^I is the maximum stress that the matrix-particle interface can undergo without decohesion; σ_c^P is the particle strength. This formulation was obtained by analyzing non-deformable inclusions in a perfectly plastic or elastic matrix. In addition, there was no particle size or inclusions interaction effects.
- Pineau and co-workers [40] proposed an improved stress-based criterion, which accounts for the plastic strain incompatibility between matrix and particle as well as the particle shape effect. This criterion is based on the generalization to an elastoplastic matrix of the Eshelby solution (initially for the elastic case [41]) by Berveiller and Zaoui [42]. This study was carried out on an A508 steel containing elongated MnS inclusions[3]:

$$\Sigma_I^{\max} + k_s(\Sigma_{eq} - \sigma_0) = \min(\sigma_c^I, \sigma_c^P) \tag{9}$$

  where $\Sigma_I^{\max}$ is the remote maximum principal stress; σ_0 is the matrix initial yield strength; k_s is a factor depending on particle shape and loading direction; $k_s(\Sigma_{eq} - \sigma_0)$ defines the internal stress, which arises from the strain inhomogeneity between inclusion and matrix. Note that in [40], these authors used this criterion to predict the decohesions both by inclusions failure (in longitudinal direction - loading direction of their tensile test on notched round bar) and by interface debonding (in transverse direction). The stress fields are considered as homogeneous within the particle both in Eqs. 8 and 9.
- More accurate prediction can be obtained by the studies of Lee and Mear [44, 45], in which the stress concentration factors at interface and inside the particle were employed to formulate the nucleation criteria:

$$\kappa_I = \frac{\max(\sigma_{\eta\eta}|_{\eta=\eta_0})}{\Sigma_{33}}; \quad \kappa_P = \frac{\max(\sigma_I^P|_{\eta\leq\eta_0})}{\Sigma_{33}} \tag{10}$$

  where Σ_{33} is the remote axial stress; $\sigma_{\eta\eta}|_{\eta=\eta_0}$ is the normal stress at the matrix-particle interface ($\eta = \eta_0$, where η defines a spheroidal coordinate, which allows locating the confocal ellipses); $\sigma_I^P|_{\eta\leq\eta_0}$ is the maximum principal stress in the particle volume ($\eta \leq \eta_0$). The two factors κ_I and κ_P depend on different factors, such as rheology parameters (e.g., Poisson's ratio[4], rigidity mismatch, hardening coefficient of matrix, matrix yield strength), morphology parameters (e.g., particle aspect ratio, particle size), loading (the remote stress triaxiality). Stress concentration inside the particle is always greater than that at matrix-particle interface as soon as plastification occurs.

A review of the nucleation aspect in ductile fracture based on micromechanical approach can be found in Appendix A of [43] or in [2], in which the influence of

[2] In Fig. 2a, at low stress triaxiality ($\eta < 1$), a change of the stress triaxiality leads to a more significant change of E_c than at higher stress triaxiality.

[3] MnS inclusions are soft inclusions, which are two times softer than steel matrix. The inclusion in a matrix is said *soft* when its yield stress is smaller than that of matrix. In the other case, it is said *hard*. The ratio between the particle yield stress and the matrix yield stress is called the *relative plasticity* [43].

[4] Poisson's ratio was shown to have minor influence [44].

different factors (*relative plasticity*, *particle size*, *rigidity mismatch*, etc.) was discussed in detail.

Besides the energy and stress-based criteria, strain-based criteria for nucleation have also been extensively developed. Needleman and Rice [46] developed a phenomenological model for nucleation, where the void nucleation is governed by the equivalent plastic strain of the matrix and the hydrostatic stress (or the mean stress σ_m):

$$\dot{f}_{\text{nucleation}} = A\dot{\overline{\epsilon}}_p + B\dot{\overline{\sigma}}_m \tag{11}$$

where A and B are two parameters, which are non-constant, $\dot{f}_{nucleation}$ is the rate of void volume change due to nucleation. If the nucleation is only due to macroscopic stress, $A = 0$ and $B > 0$. With this approach, a normal distribution formulation for B was proposed [46]:

$$B = \frac{f_N}{S_N\sqrt{2\pi}} \exp\left[-\frac{1}{2}\left(\frac{(\overline{\sigma}+\sigma_m)-\sigma_N}{S_N}\right)^2\right] \tag{12}$$

where f_N is the total void volume fraction created by nucleation, σ_N is the average stress at maximal nucleation, S_N is the standard deviation of normal distribution, $\overline{\sigma}$ is the von Mises equivalent stress (also the flow stress of matrix for J_2 plasticity). If the void nucleation is only controlled by plastic strain, $B = 0$ and $A > 0$. Chu and Needleman [9] defined A as a normal distribution:

$$A = \frac{f_N}{S_N\sqrt{2\pi}} \exp\left[-\frac{1}{2}\left(\frac{\overline{\epsilon}_p-\epsilon_N}{S_N}\right)^2\right] \tag{13}$$

where ϵ_N is the average plastic strain at maximal nucleation; f_N and S_N have the same meaning as above. As stated in [47], the main difference between the strain and stress driven nucleation is that the hydrostatic pressure has been accounted for in the latter formulation. The proposed values of [9] for A and B were then taken to describe the void nucleation in the GTN model (see Section "Gurson-like limit analysis kinematic approach" for more details).

Void growth

After nucleation, voids will grow by plastic deformation and hydrostatic stress then finally link together. Many models have been proposed in the literature to model the void growth process within a perfect plastic matrix, e.g., Rice's formulation [6] - Eq. 14 (which was then modified by Huang [48] - Eq. 15), or Gurson constitutive model [7].

$$\frac{dR}{R} = 0.272\exp\left(\frac{3}{2}\eta\right)d\overline{\epsilon}_p \tag{14}$$

$$\frac{dR}{R} = \begin{cases} 0.427\eta^{0.25}\exp\left(\frac{3}{2}\eta\right)d\overline{\epsilon}_p & if \quad \eta \le 1 \\ 0.427\exp\left(\frac{3}{2}\eta\right)d\overline{\epsilon}_p & if \quad \eta > 1 \end{cases} \tag{15}$$

The growth and coalescence processes depend on loading conditions and materials microstructure. Thomason [49] showed that for low stress triaxiality cases, ductile fracture is due to large shape changing growth and relatively small volume changing growth. From the fact that voids nucleate over a large range of plastic strain, the nucleation and growth stages occur simultaneously, which leads to the formation of voids with different sizes and shapes. Moreover, when a very small void is located near a much larger void, the growth rate of the small void is significantly increased due to the strain concentration developing around the neighbor larger void [50].

Void coalescence

Voids coalescence is the final stage of damage and ductile failure. Three modes of coalescence have been observed: (1) the "internal necking mode" (necking of matrix between two voids - see Fig. 3a-e); (2) the "shear localization mode" (reduction of the inter-particle spacing during large rotation of matrix under relatively low stress triaxiality - see Fig. 3f-j), "necklace coalescence" (a less common mode, which is caused by localization process in the main loading

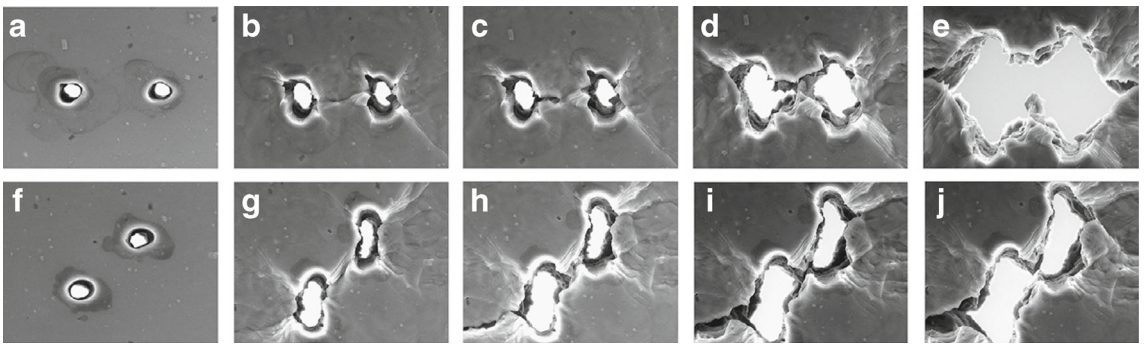

Fig. 3 Illustration of 2 modes of coalescence: **a-e** internal necking; **f-j** shear localization [52]. Reprinted from [52] with permission from Elsevier

Table 1 Several coalescence models in the literature (see also [53])

Authors	Criteria	Material matrix	Limitations
McClintock [5]	Hole impingement	Plastic With or without hardening	Cylindrical holes No interaction between holes No localization
Brown&Emburry [54]	Void length equals inter-void spacing	No hardening	Regular array of voids No influence of the stress triaxiality Overestimation of fracture strain
Tvergaard&Needleman [12]	Critical void volume fraction	Hardening	Average measurement Phenomenological method
Thomason [55]	Limit plastic load No coalescence occurs for very flat voids	No hardening	Damage growth is neglected
Pardoen&Hutchinson [15]	Thomason's model with strain hardening GLD model for void growth	Hardening	No shear localization
Benzerga [16]	Heuristic extension of Thomason's model Valid for flat voids Complete model for post-localization	Hardening	No shear localization
Benzerga&Leblond [18]	Rigorous analyses similar to Thomason's work A closed-form yield criterion for incipient failure	Hardening	Only predominately tensile triaxial stress

axis direction [43, 51]). For ductile metals, voids can double or even triple in size before their coalescence, while for less ductile materials, this process starts immediately after nucleation.

Several models were developed in the literature to model the coalescence as well as post-coalescence behavior (see Table 1). These models are based principally on cell computations with the presence of initial voids, which are generally 2D (cylindrical voids) or axisymmetric. The geometrical parameters involved are: (1) void aspect ratio and (2) relative inter-voids distance. Detailed analytical formulations are not recalled here, interested readers can refer to [53] or [2] for the reviews of different coalescence models in the literature. Zhang et al. [47] employed the Thomasson coalescence criterion, the GTN yield surface and the post-coalescence response proposed by Tvergaard and Needleman [11, 12] to achieve the so-called "complete Gurson model"[5].

In the above analyses, the results were obtained by the studies of isolated voids or a limited number of voids. In reality, the presence of numerous voids can modify the overall behavior [56, 57]. Pardoen et al. [51] showed that the voids distribution has a strong influence on the void coalescence onset while this effect can be neglected during the void growth process. The coalescence phase depends not only on the overall voids volume fraction, but especially the distance between voids. The latter parameter has been shown to have significant influence on ductile fracture by several recent experimental results (e.g., [58]).

Mechanisms dominating at negative or positively low stress triaxiality

In contrast to high stress triaxiality regime, ductile damage under negative stress triaxiality range has been received less attention. However, negative stress triaxiality is often encountered in many forming processes involving dominant compressive loadings. The upsetting test is often used to study the ductile crack formation in the negative stress triaxiality range as in the work of Bao and Wierzbicki [59] or Zapara et al. [60] and Tutyshkin et al. [61][6]. From the examination of fracture surface, Bao and Wierzbicki showed that there is no evidence showing cracked particles and nucleated voids, the fracture surface is relatively smooth in comparison with dimpled surface under high stress triaxiality. The damage process and crack formation is thus due to a different mechanism from the well-known mechanisms of void nucleation, growth and coalescence. However, from their numerical simulations, Cao et al. [62] revealed that the stress state at a material point on the surface of the compressed cylinder could change from a state of $\eta < 0$ to $\eta > 0$ during the compression test. Kweon and co-workers [63, 64] used combined Digital Image Correlation (DIC)

[5]The word "complete" refers to the capacity of this model to simulate the whole process of ductile fracture, from void nucleation to void coalescence.

[6]In the studies of Zapara et al. [60] and Tutyshkin et al. [61], the cylindrical specimens contained artificial voids, i.e., drilled holes were used, which allowed describing more accurately the fracture mechanisms in their upsetting tests (due to the difficulty of observing real voids inside the normal cylindrical sample under compression).

experiment and crystal-plasticity simulations to reveal the damage mechanisms at zero and negative stress triaxiality at mesoscale (i.e., at grain level). According to these authors, damage at this triaxiality regime is due to grain to grain interaction, which leads to the development of hydrostatic tensile stress inside grain. They incorporated this mechanism into a crystal-plasticity-based damage model.

More recently, Achouri et al. [65] carried out detailed SEM observations of voids development in a shear-dominated stress state region obtained with a shear test on a high-strength low-alloy steel (HSLA steel), where the stress triaxiality is low or zero. These authors observed the void nucleation due to different mechanisms: (1) debonding around an inclusion (Fig. 4a), (2) cracking inside a particle (Fig. 4b) or (3) mixed mode (i.e., both matrix-particle debonding and particle cracking took place Fig. 4c).

From Fig. 4a, one can observe that in the undeformed state (i.e., 0 %), the matrix and the inclusion were "coherent". Then, under shear loading, matrix-particles debonding occurred at interface and then void grew in a non-uniform manner in both shear directions, forming "corners" (in comparison with elongated void in loading direction, developed under tensile loading). These authors also mentioned the void rotation in these shear tests, depending on loading level, which was not observed in their tensile test.

For low stress triaxiality cases, the ductility or the strain to fracture can be approximated as the strain corresponding to the void coalescence onset, while this approximation must be used with caution for high triaxiality range. The ductile fracture process due to the development of voids can be split into two stages: homogenous deformation (nucleation and growth) and localized deformation due to the voids coalescence [47]. Since the void growth rate is proportional to the exponential of stress triaxiality [6], the strain to fracture decreases with the increase of stress triaxiality at a given Lode parameter (Fig. 2b).

Reviews on damage models

Different damage models proposed in the literature can be classified into three main approaches:

1. failure criteria (uncoupled damage models),
2. continuum damage mechanics (CDM - coupled phenomenological models),
3. micromechanics-based models.

Failure criteria - Uncoupled damage model

In the first approach, failure is predicted to occur when one external variable (uncoupled from other internal variables, e.g, plastic strain) reaches a critical value. However, the calculated damage does not interact with materials elasto-plastic properties. Damage variable is, therefore, just a "warning" for the approach of failure. Thanks to its simplicity, this approach was increasingly developed, especially for industrial applications.

Initially, the uncoupled damage models were based on physical assumptions, in which the damage parameters were linked with void growth (e.g., [5, 6, 66]). These models do not take into account the presence of inclusions. Moreover, the McClintock and Rice & Tracey models are based on the analysis of an isolated cavity in an elastoplastic matrix and neglect the interaction between different cavities. Bao

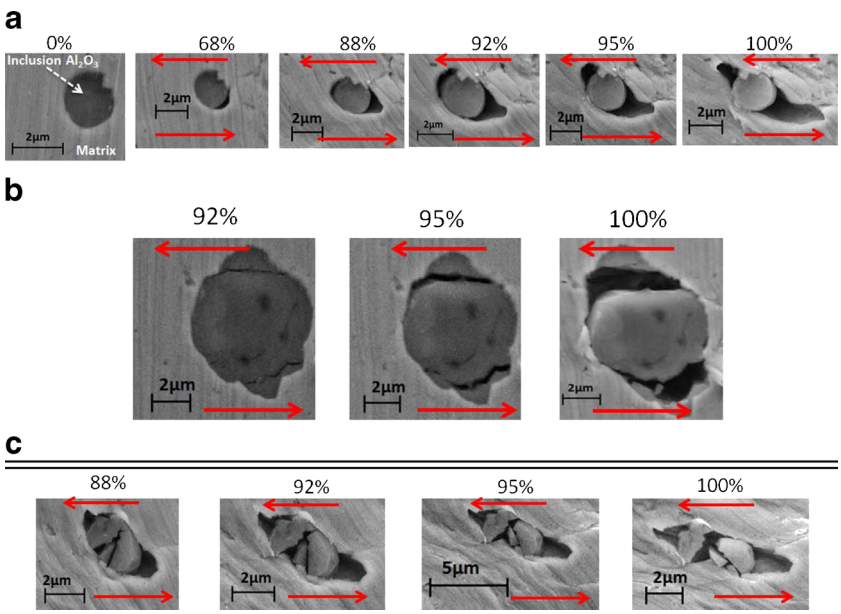

Fig. 4 SEM observations of the development of voids due to **a** matrix-particle decohesion; **b** particle cracking; (3) mixed mode. The percentages correspond to the percentage of displacement to fracture and the red arrows represent the loading direction. Reprinted from [65] with permission from Elsevier

Table 2 Uncoupled phenomenological models

Model-Authors	$f(\boldsymbol{\sigma})$
McClintock-[5]	$\frac{\sqrt{3}}{2(1-n)}\sinh\left(\frac{\sqrt{3}}{2(1-n)}\frac{\sigma_1+\sigma_2}{\bar{\sigma}}\right)+\frac{3}{4}\frac{\sigma_1-\sigma_2}{\bar{\sigma}}$
Cockcroft-Latham (CL)-[72]	$<\sigma_1>$
Rice&Tracey (RT)-[6]	$\exp(\frac{3}{2}\eta)$
Wilkin et al. -[73]	$\frac{1}{(1-a_1\sigma_m)^{\lambda}}(2-A)^{a_2},\quad A=\max\left(\frac{s_2}{s_1},\frac{s_2}{s_3}\right)$
Johnson-Cook-[74]	$1/\bar{\epsilon}_f$, with $\bar{\epsilon}_f = C_1 + C_2\exp(-C_3\eta)$
Xue&Wierzbicki-[75]	$1/\bar{\epsilon}_f$, with $\bar{\epsilon}_f = C_1\exp(-C_2\eta) - (C_1\exp(-C_2\eta) - C_3\exp(-C_4\eta))\left(1-\xi^{1/n}\right)^n$
Bai&Wierzbicki-[31]	$1/\bar{\epsilon}_f$, with $\bar{\epsilon}_f = \left[\frac{1}{2}\left(\bar{\epsilon}_f^{(+)}+\bar{\epsilon}_f^{(-)}\right)-\bar{\epsilon}_f^{(0)}\right]\bar{\theta}^2+\frac{1}{2}\left(\bar{\epsilon}_f^{(+)}-\bar{\epsilon}_f^{(-)}\right)\bar{\theta}+\bar{\epsilon}_f^{(0)}$ $\bar{\epsilon}_f^{(+)} = D_1e^{-D_2\eta}, \bar{\epsilon}_f^{(0)} = D_3e^{-D_4\eta}, \bar{\epsilon}_f^{(-)} = D_5e^{-D_6\eta}$
MMC- [68]	$1/\bar{\epsilon}_f$, with $\bar{\epsilon}_f = \left(\frac{\sqrt{3}K}{c_2}\left[\sqrt{\frac{1+c_1^2}{3}}\cos(\frac{\bar{\theta}\pi}{6})+c_1\left(\eta+\frac{1}{3}\sin(\frac{\bar{\theta}\pi}{6})\right)\right]\right)^{-1/n}-\epsilon_0$
Extended CL- [76]	$1/W_c\left\langle\frac{\phi(3\eta\sqrt{3+\mu^2}-3-\mu)+6}{3\sqrt{3+\mu^2}}\right\rangle^{\gamma}\bar{\sigma}$
Extended RT- [76]	$\frac{\ln(f_c/f_0)}{3\kappa_g\exp(\psi\eta)+\kappa_s f\left(1-(9\mu-\mu^3)^2/(\mu^2+3)^3\right)}$
Lou et al.- [69]	$\left(\frac{2}{\sqrt{\mu^2+3}}\right)^{C_1}\left(\frac{\langle 1+3\eta\rangle}{2}\right)^{C_2}$
Lou et al.- [77]	$\left(\frac{2}{\sqrt{\mu^2+3}}\right)^{C_1}\left\langle\frac{1}{1+C}\left(\eta+\frac{3-\mu}{3\sqrt{\mu^2+3}}\right)\right\rangle^{C_2}$

and co-workers [67], in a comparative study, showed that different functions are necessary to predict crack initiation for different ranges of stress triaxiality, and that it is impossible to capture all features of ductile fracture for different stress states with a single stress triaxiality-based criterion. The above-mentioned models were shown to be valid for specific loadings and depend strongly on the strain path.

Beside the physically-inspired uncoupled models, many other models were phenomenologically constructed and the damage indicator was not linked with any physical property. The damage parameter is often defined as a cumulative function along the strain path:

$$\int_0^{\bar{\epsilon}_f} f(\boldsymbol{\sigma})\, d\bar{\epsilon}_p = D_c \tag{16}$$

where $f(\boldsymbol{\sigma})$ is a function of the stress state; D_c is a material constant that defines the onset of fracture; $\bar{\epsilon}_f$ is the equivalent strain at fracture. We can name here some criteria: hydrostatic stress ($f = \frac{\sigma_m}{\sigma_{eq}}$) and Oyane ($f = a + b\frac{\sigma_m}{\sigma_{eq}}$) among others. These criteria are reliable in predicting fracture only if the parameters of function f are measured from mechanical tests which are close to the studied processes, regardless of damage anisotropy. The pioneer works, e.g., by [6], accounts only for the stress triaxiality in the function $f(\boldsymbol{\sigma})$, but recently proposed fracture criteria (e.g., [31, 68–71]) take into account also the Lode parameter. The common idea of these works is to construct the strain to fracture as a function of the stress triaxiality and the Lode parameter, at least for proportional loadings. Table 2 summarizes several uncoupled models proposed in the literature, accounting only for stress triaxiality or both stress triaxiality and Lode parameter ($\bar{\theta}$ or μ - see Eqs. 6 and 7).

In these formulations n is the hardening exponent; ξ is the normalized third stress invariant, defined in Eq. 4; $\sigma_1, \sigma_2, \sigma_3$ are three principal stresses; s_1, s_2, s_3 are three principal stress deviators; f_0 and f_c are respectively the initial and critical (i.e., at fracture) void volume fractions; a_1, a_2, C_1, C_2, C_3, C_4, D_1, D_2, D_3, D_4, D_5, D_6, c_1, c_2, W_c, ϕ, ψ, κ_g, κ_s, C are fitted parameters. Uncoupled damage models were initially based on an assumption of proportional or radial loadings to define the so-called strain to fracture function ($\bar{\epsilon}_f$). For a non-proportional loading, the use of average measurements[7] to construct a fracture locus does not make sense since these measurements cannot account for the whole loading history (e.g., a cyclic tension-compression test on axisymmetric specimen). In the study of Bai and Wierzbicki, the authors constructed the fracture loci based on their "proportional" experiments. Moreover, they transformed the stress-based M-C criterion, to a mixed strain/stress-based formulation to predict fracture. This transformation is valid only if the loading is proportional. Recently, Benzerga and co-workers [78] examined the influence of strain history on fracture behavior by using cell model calculation. In their simulations, these authors considered two cases: radial loading and non-radial loading. For the latter case, loading was composed of two

[7] $\overline{\eta}_{av} = \frac{1}{\bar{\epsilon}_f}\int_0^{\bar{\epsilon}_f}\eta(\bar{\epsilon}_p)d\bar{\epsilon}_p, \overline{\theta}_{av} = \frac{1}{\bar{\epsilon}_f}\int_0^{\bar{\epsilon}_f}\bar{\theta}(\bar{\epsilon}_p)d\bar{\epsilon}_p$ are respectively the strain-averaged values of the stress triaxiality and the Lode parameter.

steps. In each step, the stress triaxiality was kept constant (i.e., a piecewise constant function) and the strain-averaged value of the stress triaxiality was equivalent to the case of radial loading. By varying the stress triaxiality, these authors showed that for each value of average stress triaxiality, the value of "fracture strain" was not unique. The application of these criteria for non-proportional loading needs further consideration about the meaning of the function $\overline{\epsilon}_f$. In this case, $\overline{\epsilon}_f$ is no longer the strain to fracture function, but rather a weighting function, which accounts for the stress state. Uncoupled damage models (or fracture criteria) can be based on physical assumptions (e.g., Rice and Tracey criterion) or purely phenomenological assumptions, in which damage parameter is defined as an integration of a stress-based function along the strain path: $D = \int_0^{\overline{\epsilon}_p} f(\boldsymbol{\sigma})\, d\overline{\epsilon}_p$. If the stress-based function $f(\boldsymbol{\sigma})$ is chosen as: $f(\boldsymbol{\sigma}) = 1/\overline{\epsilon}_f$, with $\overline{\epsilon}_f$ defined as in the formulations shown in Table 2 and if proportional (or nearly proportional) tests are used to calibrate these models, this function $\overline{\epsilon}_f$ *coincides* with the fracture strain. To summarize, $\overline{\epsilon}_f$ must not be considered as a fracture strain function in a strict sense. It is only a phenomenological weighting function, which *coincides* with the fracture strain for radial loadings. The fracture prediction in numerical simulation is based on the damage variable D. Generally, the uncoupled models have the advantages of being easy to implement in FE software and having few parameters to identify. The application to complex loading paths outside the identification zone and large plastic deformation is their major weakness (see the detailed discussion in Section 5.2 of [62]).

Continuum damage mechanics (CDM)

In the second approach, damage is associated with one of the internal constitutive variables that accounts for the influence of the irreversible process occurring in materials microstructure. This approach is a phenomenological representation of the CDM that was first initiated by Kachanov [79] for creep damage. They are considered as "phenomenological" because their developments are essentially based on macroscopic considerations. However, these models are based on a consistent thermodynamic framework, which ensures a non-negative dissipation. This framework for ductile damage was later developed by Chaboche [80] and Lemaitre [81, 82]. Several models relative to the initial framework of Lemaitre, based on the use of special expressions for the damage dissipation potential, were developed by different authors [83–88].

The Lemaitre model is derived from the thermodynamics framework of continuum damage mechanics, which consists in three steps: (1) definition of state variables (e.g., damage variable), which define the present state of corresponding physical mechanism (i.e., damage); (2) definition of state potential, from which one can derive the state laws, and definition of associated variables (i.e., the variables which are associated with the internal state variables); (3) dissipation potential definition: to derive the evolution law of state variables, which are associated with the dissipative mechanisms. The scalar D ($0 \leq D < 1$), an internal variable, is adopted to describe the *isotropic damage* (D is assumed to represent the ratio of damaged area S_D to the total surface S of any cross section: $D = S_D/S$). The effective stress is used to describe the impact of damage on the macro-behavior of material. This stress is the one that should be applied to an undamaged material, in order to get the same strain tensor as the one obtained from the damaged material under actual stress (strain equivalence principle). The effective stress is defined as:

$$\sigma'_{ij} = \frac{\sigma_{ij}}{1 - D} \tag{17}$$

where σ'_{ij} is the component of the effective stress tensor, σ_{ij} is the component of the actual stress tensor. The effective stress is used in the constitutive equations instead of the Cauchy stress to describe the damage impact on the macroscopic behavior of materials. The energy density release rate (Y), the variable associated with D, is derived from the state potential (see [82] for more details):

$$Y = \frac{\overline{\sigma}^2}{2E(1-D)^2}\left[\frac{2}{3}(1+\nu) + 3(1-2\nu)\eta^2\right] \tag{18}$$

The contribution to the dissipational potential corresponding to damage F_D is proposed as:

$$F_D = \frac{S}{(b+1)(1-D)}\left(\frac{Y}{S}\right)^{b+1} \tag{19}$$

S (MPa) and b are two material parameters (which might depend on temperature). The damage evolution is given by:

$$\dot{D} = \dot{\lambda}\frac{\partial F_D}{\partial Y} = \frac{\dot{\lambda}}{1-D}\left(\frac{Y}{S}\right)^b = \dot{\overline{\epsilon}}^p\left(\frac{Y}{S}\right)^b \tag{20}$$

where $\dot{\lambda}$ is the plastic multiplier, which can be deduced from the equivalent plastic strain rate as: $\dot{\lambda} = \dot{\overline{\epsilon}}^p(1-D)$, with $\dot{\overline{\epsilon}}^p = \sqrt{\frac{2}{3}\dot{\boldsymbol{\epsilon}}^p : \dot{\boldsymbol{\epsilon}}^p}$ ($\dot{\boldsymbol{\epsilon}}^p$ denotes plastic strain rate tensor). Under shear-dominated loading, the stress triaxiality is zero or slightly positive, Lemaitre damage variable still increases but slower since it is based principally on the stress triaxiality (Eq. 20). As shown in [62, 89], the use of this model in shear-dominated and complex forming processes may lead to inaccurate predictions of maximum damage locations. To overcome this shortcoming, Cao et al. [62, 88] proposed a Lode-dependent Enhanced Lemaitre model, by accounting

for the following modifications (see also [90] for another approach):

1. The evolution of damage variable (see Eq. 21) was modified to account for the Lode parameter.
2. The damage threshold (ϵ_D) was modified to account for the influence of the stress triaxiality (Eq. 21).
3. The weakening function was modified to better account for the influence of damage at low stress triaxialities (Eq. 22).

The governing equations are summarized as:

$$\dot{D} = \begin{cases} \frac{\dot{\bar{\epsilon}}^p}{} \left(\frac{Y}{S}\right)^b \frac{1}{\alpha_1+\alpha_2\bar{\theta}^2} & \text{, if } \bar{\epsilon}^p > \epsilon_D = \epsilon_{D0}\exp(-A\eta) \quad \text{and} \quad \eta > -\frac{1}{3} \\ 0 & \text{, otherwise} \end{cases} \tag{21}$$

$$\begin{cases} \sigma_{ij} = w(D)\sigma'_{ij} \\ E = w(D)E_M \end{cases} \quad \text{with} \quad w(D) = \begin{cases} 1-D & \text{, if } \eta \geq \eta_1 \\ 1 - \frac{(1-h)\eta + h\eta_1 - \eta_2}{\eta_1 - \eta_2} D & \text{, if } \eta_1 > \eta \geq \eta_2 \\ 1 - hD & \text{, if } \eta < \eta_2 \end{cases} \tag{22}$$

This model has been successfully applied to predict fracture for different mechanical tests at different loading configurations both at low and high triaxialities, where the Lemaitre model gave unsatisfied results [62, 88, 91]. For more details on continuum models, interested readers can refer to a recent review of Besson [3].

Micromechanics-based damage models

This section focuses on micromechanics-based models, which can be further put into two sub-categories: (1) Gurson-like approach (Section "Gurson-like limit analysis kinematic approach") and (2) nonlinear homogenization-based approach (Section "Nonlinear homogenization based approach"). Since they are based on microstructure considerations, micromechancal computations on unit-cell are often performed to calibrate these models and also to investigate ductile fracture mechanisms (e.g., void growth and coalescence), which is the subject of Section "Cell computations".

Gurson-like limit analysis kinematic approach

In this approach, the influence of ductile damage in the yield condition is taken into account by a porosity term that progressively shrinks the yield surface, which was proposed by Gurson [7]. Further extensions of Gurson's framework were devoted to different aspects, especially that of [8, 11, 12] to improve the prediction accuracy by accounting for interaction, nucleation and final coalescence of voids (the GTN model); [19, 92] for void shape effect (the GLD model) (see 2). The yield function of the GTN model [12] writes:

$$\Phi = \left(\frac{\overline{\sigma}}{\sigma_0}\right)^2 + 2q_1 f^* \cosh\left(-\frac{3q_2}{2}\frac{p}{\sigma_0}\right) - 1 - q_3 f^{*2} = 0 \tag{23}$$

σ_0 is the flow stress of matrix material; q_1, q_2, $q_3 = (q_1)^2$ are material constants; f^* is the effective void volume fraction, which accounts for the voids' linkage:

$$f^* = \begin{cases} f & , if \quad f < f_c \\ f_c + \frac{f_u^* - f_c}{f_f - f_c}(f - f_c) & , if \quad f \geq f_c \end{cases} \tag{24}$$

where f_c represents the critical value of f at which void coalescence begins, f_f its value at ductile failure, and $f_u^* = \frac{q_1 \pm \sqrt{q_1^2 - q_3}}{q_3}$ the corresponding value of f^* at failure. The evolution of void volume fraction is described as:

$$\dot{f} = \dot{f}_{\text{nucleation}} + \dot{f}_{\text{growth}} \tag{25}$$

where $\dot{f}_{\text{growth}}$ is defined as $\dot{f}_{\text{growth}} = (1-f)\text{trace}(\dot{\boldsymbol{\epsilon}}_p)$ and $\dot{f}_{\text{nucleation}}$ is often described by a Gaussian curve that was introduced by [9] (see Section "Void nucleation"):

$$\begin{aligned} \dot{f}_{\text{nucleation}} &= \frac{f_N}{S_N\sqrt{2\pi}} \exp\left[-\frac{1}{2}\left(\frac{\bar{\epsilon}_p - \epsilon_N}{S_N}\right)^2\right]\dot{\bar{\epsilon}}_p \\ &= A\left(\bar{\epsilon}_p\right)\dot{\bar{\epsilon}}_p \end{aligned} \tag{26}$$

with:

- ϵ_N: value of mean plastic strain at maximal nucleation;
- S_N: standard deviation of the corresponding Gaussian distribution;
- f_N: the volume fraction of void that can be nucleated. This parameter is determined so that the total void volume nucleated is consistent with the volume fraction of particles [8].

The influence of the stress triaxiality on the nucleation process (as shown in [93]) can be incorporated, e.g., by adopting a stress-dependent formulation for the strain at maximum nucleation ϵ_N [94, 95]:

$$\epsilon_N = \epsilon_{N_0}\exp(-B\eta) \tag{27}$$

where η is the stress triaxiality, which can be taken as the initial stress triaxiality if the loading is nearly proportional;

[8] The volume fraction that can be nucleated is equal to $\int_0^{\infty} A(\bar{\epsilon}_p)d\bar{\epsilon}_p$, whereas $f_N = \int_{-\infty}^{\infty} A(\bar{\epsilon}_p)d\bar{\epsilon}_p$. If S_N is small enough with respect to ϵ_N, $f_N = \int_{-\infty}^{\infty} A(\bar{\epsilon}_p)d\bar{\epsilon}_p \approx \int_0^{\infty} A(\bar{\epsilon}_p)d\bar{\epsilon}_p$.

B and ϵ_{N_0} are two parameters to be identified. This modification allows the void nucleation process to take place earlier at high stress triaxialities.

The evolution of plastic strain is obtained through the equivalence of the plastic work, overall and in matrix material:

$$(1-f)\sigma_0 d\overline{\epsilon}_p = \boldsymbol{\sigma} : d\boldsymbol{\epsilon}_p \rightarrow \Delta\overline{\epsilon}_p = \frac{\boldsymbol{\sigma} : \Delta\boldsymbol{\epsilon}_p}{(1-f)\sigma_0} \tag{28}$$

where $\boldsymbol{\sigma}$ and $\Delta\boldsymbol{\epsilon}_p$ are the stress tensor and the increment of the plastic strain tensor. The evolutions of the two internal state variables ($\overline{\epsilon}_p$ and f) are summarized as

$$\Delta\overline{\epsilon}_p = \frac{\boldsymbol{\sigma} : \Delta\boldsymbol{\epsilon}_p}{(1-f)\sigma_0} \tag{29}$$

$$\Delta f = (1-f)\Delta\epsilon_p + A\left(\overline{\epsilon}_p\right)\Delta\overline{\epsilon}_p \tag{30}$$

where ϵ_p is the volumetric part of the plastic strain tensor.

The constitutive parameters q_1 and q_2 of the GTN (or GT) yield function are often chosen as proposed by [8]: $q_1 = 1.5$ and $q_2 = 1$. However, several authors re-identified these parameters to obtain more accurate results for their studies, which could be based on cell computations, classical mechanical tests or microstructural observations (see Table 3 for different values of q_1 and q_2 identified by several studies in the literature where $q_1 \neq 1.5$).

Although this model was successfully applied to predict fracture at high triaxiality, it still suffers a major limitation in pure shear loading, for which there is no void growth. In addition, the Gurson framework has also been shown to be insufficient to predict fracture at low stress triaxiality and especially shear-dominated loadings. Several modifications were proposed by [30] and [29] to include the influence of the third stress invariant through the Lode angle in the Gurson or GTN models, but these modifications are purely phenomenological. More recently, [105–107] pointed out that the independence upon the third stress invariant in the classical Gurson model is due to an approximation of this author when calculating the overall plastic dissipation. These authors proposed separately different solutions (e.g., use exact formulations for axisymmetric loading - [105], or use second and third approximations for general loading instead of the first approximation used by Gurson for a term in the derivation of the overall plastic dissipation - [107]). Cazacu et al. [105] showed that, when $p < 0$, a softer behavior than the original Gurson model is obtained when the third stress invariant is positive and the Gurson's solution is an upper bound of the new model. In addition, the resulting yield surfaces [105, 106] are non-symmetric with respect to $p = 0$. However, the difference between the models proposed by these authors and that of Gurson is small, and can be treated by using the GTN model with additional constitutive parameters q_1 and q_2, at least for quasi-static loadings; while still has the deficiencies at low stress triaxialities. The reason for this is that, all these models are based on the assumption of spherical voids that remain spherical, which is totally incorrect at low stress triaxialities.

Gologanu and co-workers [19, 92] first proposed a constitutive model with aligned spheroidal voids subjected to axisymmetric loadings, aligned with voids symmetry axis (see [2] for a recent review on its derivation and applications). The last model of [108] considered general ellipsoid. This class of models fails for general loading conditions, where loadings are not aligned with voids principal axes and important void rotation is involved. Several extensions have been proposed, especially to account for final coalescence stage [15] and void rotation [17]. Pardoen and Hutchinson [15] constructed a void growth and coalescence model by combining the GLD void growth (extended to hardening materials) with the modified Thomason coalescence model [55]. Recently, Scheyvaerts et al. [17] used the same approach and added an evolution law for void rotation proposed in [109], only for plane strain state (i.e., only

Table 3 Values of fitted parameters for q_1 and q_2 in the GTN yield function (if these parameters were identified from experiments, the materials used are also given)

Author	Material	q_1	q_2
Gurson [7]	-	1.0	1.0
Koplik and Needleman [96]	-	1.25	1.0
Xia and Cheng [97]	A533B steel	1.25	1.0
Faleskog et al. [98]	-	1.46	0.93
Steglich and Brocks [99]	-	1.2	1.0
Pardoen et al. [100]	Copper	1.47	1.0
Corigliano et al. [101]	API X60 steel	1.08	0.99
Zhang et al. [47]	-	1.25	1.0
Kim et al. [102]	-	1.586	0.91
McElwain et al. [103]	-	1.31	1.16
Nielsen and Tvergaard [104]	Aluminum AA2024	2.0	1.0
Cao et al. [94]	Pearlitic high C steel	1.494	1.0

one void aspect ratio was considered). These authors successfully validated their model for plane strain state but no results were reported for general ellipsoidal voids. Another drawback of such a model (and also the GLD and that of [108]) is that a large number of parameters is involved, in which some are totally induced from micromechanical analysis and cannot be identified from conventional mechanical tests.

Nonlinear homogenization based approach

In addition to the Gurson-like limit analysis kinematic approach, general constitutive models for porous ductile solid subjected to general three-dimensional loading conditions have also been developed by [110, 111] based on the early works of [109, 112] for viscoplastic composites, which can describe the change of void shape and orientation. Ponte Castañeda and co-workers [112–114] firstly proposed a nonlinear homogenization variational structure for composites comprising different *nonlinear* phases, which can be considered as "inclusions" and matrix. More precisely, this new structure allows for the estimation of the effective energy densities of nonlinear composites in terms of the corresponding information from linear comparison composites, which are proper linearization of the nonlinear ones. Kailasam and Ponte Castañeda [109] proposed a general constitutive theory for nonlinear composite materials with microstructure evolution as a consequence of finite-strain boundary conditions. Details on the numerical method used to implement such a model in a FE code can be found in [110]. Recently, Danas and Aravas [111] carried out a comparative study between the model proposed by [109] (namely VAR model), its modification by [111] (MVAR model) and the second order model (SOM) proposed by [115, 116]. The authors showed that the modified variational model (MVAR) gave same results at high triaxiality as the SOM model; and exact results for spherical and cylindrical shells subjected to hydrostatic loading (for which the VAR model fails). These kinds of models have the major advantage of accounting for the void shape and void rotation effects, which have been showed to be important at low stress triaxialities. The MVAR model has been shown to give fairly good estimates when compared with the SOM model, which in turn has been validated for axisymmetric unit-cell simulations principally for visco-plastic cases. Nevertheless, currently, the SOM model, although accurate, is computationally expensive, while the MVAR tends to over-predict void growth at low to moderate stress triaxialities as shown in [117]. More recently, Cao et al. [117] proposed a micromechanics-based model (namely GVAR) based on *ad-hoc* modifications of the VAR model to give sufficiently accurate results for void growth at both low and high stress triaxialities and keeping the functional form of the original Gurson model. These authors validated their model based on unit-cell computations for various loadings, void shapes and initial porosities, then applied to a 3D simulation of a tensile test on notched round bar and compared to tomography observations. For an isotropic case (i.e., spherical voids), the GVAR model writes (see [117]):

$$\left(\frac{\sigma_{eq}}{\sigma_0}\right)^2\left(1+\frac{2}{3}\alpha_g f\right)+2q_1 f\cosh\left(q_2\frac{3p}{2\sigma_0}\right)-1-q_1^2 f^2=0 \tag{31}$$

where α_g is a fitted parameters, p is the hydrostatic pressure. This model thus gives exactly the solutions as the Gurson model when $q_1 = q_2 = 1, \alpha_g = 0$; while it gives the upper bound proposed by [118] when $q_1 = q_2 = 1, \alpha_g = 1$. It should be noted that, both studies of Ponte Castañeda [112] and of Garajeu and Suquet [118] proposed respectively two upper bounds of the overall yield surface of porous media; while Sun and Wang [119] gave a lower bound (see [57]). Table 4 presents the yield functions for different models for an isotropic case: Gurson, Gurson and Tvergaard (G&T - [8]), Sun and Wang (S&W - [119]), VAR [109, 112–114], Garajeu and Suquet (G&S - [118]), MVAR [111] and

Table 4 Yield functions for porous materials for the spherical void

Model - Author	Yield function
Gurson - [7]	$\Phi=\left(\frac{\sigma_{eq}}{\sigma_0}\right)^2+2f\cosh\left(\frac{3p}{2\sigma_0}\right)-1-f^2=0$
G&T - [8]	$\Phi=\left(\frac{\sigma_{eq}}{\sigma_0}\right)^2+2q_1 f\cosh\left(q_2\frac{3p}{2\sigma_0}\right)-1-q_1^2 f^2=0$
S&W - [119]	$\Phi=\left(\frac{\sigma_{eq}}{\sigma_0}\right)^2+\left(2-\frac{1}{2}\log(f)\right)f\cosh\left(\frac{3p}{2\sigma_0}\right)-1-f(1+\log(f))=0$
VAR - ([109, 112–114])	$\Phi=\left(\frac{\sigma_{eq}}{\sigma_0}\right)^2\left(1+\frac{2}{3}f\right)+f\left(\frac{3p}{2\sigma_0}\right)^2-(1-f)^2=0$
MVAR - ([111])	$\Phi=\left(\frac{\sigma_{eq}}{\sigma_0}\right)^2\left(1+\frac{2}{3}f\right)+f\left(\frac{1-f}{\sqrt{f}\log(1/f)}\right)^2\left(\frac{3p}{2\sigma_0}\right)^2-(1-f)^2=0$
G&S - ([118])	$\Phi=\left(\frac{\sigma_{eq}}{\sigma_0}\right)^2\left(1+\frac{2}{3}f\right)+2f\cosh\left(\frac{3p}{2\sigma_0}\right)-1-f^2=0$
GVAR - ([117])	$\Phi=\left(\frac{\sigma_{eq}}{\sigma_0}\right)^2\left(1+\frac{2}{3}\alpha_g f\right)+2q_1 f\cosh\left(q_2\frac{3p}{2\sigma_0}\right)-1-q_1^2 f^2=0$

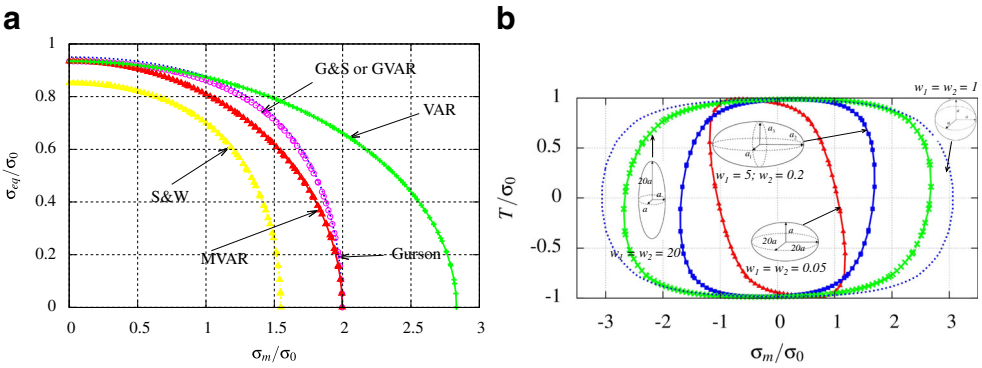

Fig. 5 **a** Comparison between different yield surfaces for porous materials for the spherical void ($f = 0.05$); **b** GVAR yield surfaces for "severe" microstructures for $f = 0.01$: prolate ($w_1 = w_2 = 20$); oblate ($w_1 = w_2 = 0.05$) and a general ellipsoid ($w_1 = 5$, $w_2 = 0.2$). For the GVAR model, all three constitutive parameters are fixed $q_1 = q_2 = \alpha_g = 1$. In (b), $|T| = \sigma_{eq}$

GVAR [117] [9]; while Fig. 5a shows the comparison of yield functions between these models for $f = 0.05$.

As can be observed in Fig. 5a at low stress triaxiality (e.g., when $\sigma_m/\sigma_0 < 1$), the Gurson model (blue curve) violates the upper bounds predicted from both G&S and VAR models. The GVAR model with $q_1 = q_2 = \alpha_g = 1$, coincides with the upper bound of [118]. The VAR model is too stiff, while MVAR is not accurate enough for low to moderate stress triaxialities (see [117]). Fig. 5b shows the comparison between yield surfaces obtained with the GVAR model for different types of void shape: spherical, oblate, prolate and general ellipsoidal voids for axisymmetric loading and for a same initial porosity $f = 0.01$. As can be observed, void shape has a strong influence on the overall behavior of porous materials.

Cell computations

Micro-mechanical analyses of ductile fracture are often performed by investigating a representative volume element (RVE) containing a single void or particle. Some of the early pioneering works focused on a square array of cylindrical voids ([8, 120]), spherical voids ([96, 98, 121, 122]) or for spherical particles ([123]) initially embedded in a ductile matrix (rigid plastic or hardening). Cell computations have been extensively used to study ductile fracture mechanisms (void growth, nucleation and coalescence - e.g., [34, 124–127]); to reveal the influence of stress states on material ductility (e.g., [35, 36]); and also to calibrate and validate micromechanically based damage models (see, e.g., [17, 117, 128]).

Figure 6 shows the cells containing one single void that are often used for computations: for triaxial loadings - spherical void (Fig. 6a); for shear and combined loadings - spherical void (Fig. 6b) and for triaxial loading on general ellipsoidal void (Fig. 6c). For the computations on these cells, fully periodic boundary conditions (BCs) are applied, in which the displacement associated with each material point $\vec{x}$ takes the following form

$$\vec{u} = (\boldsymbol{F} - \boldsymbol{I}).\vec{x} + \vec{v}, \quad \forall \vec{x} \in V_t \tag{32}$$

where $\boldsymbol{F}$ is the gradient of the displacement; $\boldsymbol{I}$ is the second order identity tensor; $\vec{v}$ is the periodic fluctuation vector, which is identical for two points located on opposite outer boundary surfaces of the total volume V_t.

Computations on unit-cell containing one single void is often used to study the ductile damage mechanisms (see Table 5 for a summary of different studies in the literature based on cell computations). These computations have also been used to calibrate micromechanics-based models. In addition, based on cell computations, the influence of void shape, stress states (i.e., stress triaxiality, Lode parameter) on void growth and coalescence can be obtained.

Figure 7 shows several important results obtained from unit cell computations ([117]). First, Fig. 7a reveals the dependency of the localization porosity f_c upon the stress triaxiality and Lode parameter. These dependencies suggest that f_c cannot be considered as a material parameter since it depends strongly on loading. Fig. 7b shows the evolution of void volume fraction for three different initial void shapes for $\eta = 0.667$ ($f_0 = 10^{-2}$). The GVAR model (continuous lines) is used to compare with cell results (dashed lines - only the pre-coalescence part is considered). As expected, at a same initial value of porosity, the void growth rate is smallest for the case of prolate void, and is highest for the case of oblate void. At this low stress triaxiality level, the influence of void shape is noticeable, which can be explained through the load bearing surface perpendicular to the loading direction. This surface is smallest for the case of oblate void (due to the largest projection surface of void in the main loading direction) and is largest for the prolate void (smallest projection surface of void in the main loading direction). This result suggests an important role of the projection surface of the void in the main loading direction on void growth rate.

In order to illustrate this idea, two cell models containing prolate and oblate voids respectively, with a same projection

[9] The VAR, MVAR, and GVAR models handle also general ellipsoidal voids.

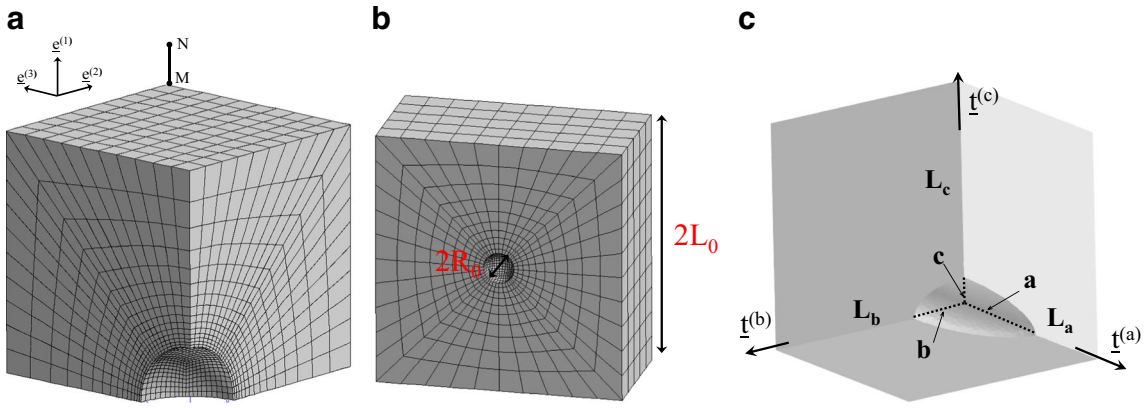

Fig. 6 **a** spring-loaded cell; **b** sheared cell for simple shear; and **c** general ellipsoidal void embedded in a unit-cell with 3 principal axes: minor (direction $\underline{t}^{(c)}$), middle (direction $\underline{t}^{(b)}$) and major (direction $\underline{t}^{(a)}$). L_a, L_b and L_c are cell's lengths; whereas a, b and c are voids semi-axes in three directions $\underline{t}^{(a)}$, $\underline{t}^{(b)}$ and $\underline{t}^{(c)}$ respectively

surface onto the plane perpendicular to loading directions, are considered (see Fig. 7c). These two voids have the same initial projection surface as the spherical void with $f_0 = 0.01$ (for this void volume fraction and with the use of the unit-cell $L_0 = 1$, the radius of the projection area is $0.02\ L_0$). This radius corresponds to the minor axis of the prolate void; while it corresponds to the major axis of the oblate void. Therefore, the initial void volume fractions are $f_0 = 0.02$ for the equivalent prolate void and $f_0 = 0.005$ for the equivalent oblate void. Loading is prescribed to have the stress triaxiality equal 2/3 (in order to have a dominant loading axis - see Fig. 7d).

In these examples, the void growth model is in good agreement with cell results for both cases. In addition, although initial porosity and void shape are different in these two cases, the rate of porosity change (i.e., the slope of these curves) is similar, which can be observed from cell results and can also be predicted by the GVAR void growth model [117]. This result suggests that, at low to moderate triaxialities, regarding the rate of porosity evolution, it is important to consider the projection of void onto the plane perpendicular to the main loading axis (see also [19]).

These cell computation results have also been employed to validate and calibrate the models for porous materials (e.g., Gurson, GTN or GLD models). It should be noted that, recent 3D simulations of [56, 57] showed that, in order to have a cell model that is representative, the number of cavities inside the cell should be high enough. From their results with 5–200 spherical cavities inside the cell, Fritzen et al. [56] proposed a modification for the constitutive parameters of the GTN model as

$$q_1(f) = 1.69 - f, \quad q_2 = 0.92 \tag{33}$$

This modification was recently verified by Khdir et al. [57] for cell containing high number of voids.

Experiments and models calibration

Experiments for damage study

Bridgman, one of the first scientists who carried out systematic fracture tests under pressure, in his famous book [129], presented all the experimental data obtained from axisymmetric tensile tests under hydrostatic pressure for 20 different types of steels. To reveal the nature of fracture in these tests, it is convenient to work with the stress triaxiality. The statistics of the average stress triaxiality of all these tests provided a global view of the limit between fracture and non-fracture zones, which is used to deduce the so-called cutoff value of the stress triaxiality, below which fracture does not occur [59]. Kao et al. [93], with the same type of tests, in the study on tensile fracture of 1045 spheroidized steel under hydrostatic pressure, clearly demonstrated that the influence of superimposed hydrostatic pressure of tensile fracture of 1045 spheroidized steel was such that void nucleation was suppressed, leading to larger post-uniform strain under pressure and a transition of the fracture surface from cup-cone mode under atmospheric pressure to a slant mode under high pressure (see Fig. 3 of [93]). However, according these authors, the maximum pressure applied (1120 MPa) was not high enough to completely suppress void nucleation around carbide particles. They revealed that the increase of the superimposed hydrostatic pressure (or the decrease of the stress triaxiality) may lead to the increase of "nucleation strain"[10]. This study also demonstrated that the increase of pressure led to a significant increase in ductility and a slight increase in flow stress. Peng and co-workers [130] numerically studied the effect of superimposed hydrostatic pressure on fracture in round bar, using FE simulations

[10]This observation was later taken into account by [94] to modify the nucleation strain of the GTN model.

Table 5 Several studies on cell computations

Authors	Material parameters	Models	Main results
Koplik and Needleman [96]	$f_0 = 0.0013$, q_1=1.25, q_2=1, f_c=0.03, f_f=0.13	Axisymmetric cell	– At low η ($\eta = 1$), Brown and Emburry [54] coalescence criterion provides good results – f_c varies slowly with η and matrix strain hardening; while it depends strongly on f_0 – q_1 increases when the strain hardening decreases
Brocks et al. [122]	$f_0 = 0.0013$, $q_1 = 1.15$, $q_2 = 1$, $f_c = 0.033$, f_f=0.15;for 2nd population: $f_N = 0.004$, $s_N = 0.1$, $f_c = 0.15$, $f_f = 0.25$, $\epsilon_N = 0.3$ or 0.8.	Spring-loaded axisymmetric cell; two populations of voids	– Less significant strain-rate effect on f_c; f_c increases when η decreases. The influence of f_c on temperature is less pronounced when f_0 is small – High η, less influence of the second population; high ϵ_N ($\epsilon_N = 0.8$): less influence of the second population (primary voids prevail). It should be important to account for the influence of η on ϵ_N (as done lately, e.g., by [94])
Kuna and Sun [124]	2nd population of voids: $q_1 = 1.5$, $q_2 = 1$, $f_0 = 0$, $f_N = 0.008$, $s_N = 0.1$, $\epsilon_N = 0.3$, $f_c = 0.04$, $f_f = 0.195$	3D cell models: cubic primitive, body centered cubic and hexagonal structure (equivalent to axisymmetric cell)	– Voids arrangement: weak influence on deformation behavior; strong influence on peak load and plastic collapse mechanism – f_c is less influenced by η – Axisymmetric cell model yields softer deformation behavior, resulting in a lower fracture stress than 3D models. Using axisymmetric cell leads to a higher identified value for q_1 and a lower one for f_c (compared to 3D models)
Needleman et al. [232] - Voids shape and size evolution in creeping solids		Axisymmetric cell	– The deviation from a spheroidal shape is rather small until necking down between voids occurs – Modification of formulation for void growth rate in viscous solids proposed by [66]
Pardoen and Hutchinson [15] - GLD for void growth and modified Thomasson for void coalescence	Hardening plastic solid	2D axisymmetric cell	– Effect of the cell aspect ratio χ_0: same f_0, w_0, the increase of χ_0 leads to early localization + steeper unloading curve after localization onset (due to elastic unloading) – Influence of void shape on f_c: more pronounced at low η (when $f_0 \approx 0.01$). At low f_0, less influence of shape on f_c – Hardening: low η, f_c weakly depends on n (hardening coefficient); high η, f_c increases when n increases – Coalescence model: accounts for the influence of χ_0 (post-localization, steeper slope). For low η, the model must account for the influence of inclusions

Table 5 (continued)

Authors	Material parameters	Models	Main results
Barsoum and Faleskog [33, 34] - Void growth under combined shear and tension	Hardening plastic solid	3D cell + periodic BCs	– Lode parameter influence on void growth and coalescence can be significant, especially at low η – Two fracture mechanisms can be predicted with micromechanical models. Shear failure is predicted by a critical shear deformation criterion and pre-existing voids do not play a significant role
Tvergaard [233] - Localization of 2D cell containing a single void subjected to shear dominated stress state	Hardening plastic solid	2D cell, cylindrical voids, plane strain, periodic BCs + remeshing. Internal pressure was added to represent the interaction between void surfaces in frictionless sliding	– Load maximum in a strain hardening material leading to failure under pure shear or shear-dominated loadings was observed – Void surfaces contact occurred well before the load maximum, so that the void surfaces contact appeared to be an important part of the mechanism leading to plastic flow localization – 3D numerical analysis should be performed for more realistic results
Tvergaard [234] - As in [233], but the internal load on the void surface does not have a component in the direction along the elongated void	Hardening plastic solid	2D cell, cylindrical voids, plane strain, periodic BCs + remeshing. Internal load was added to represent interaction between void surfaces in frictionless sliding	– Load maximum occurred later than that found in [233], using internal pressure – Void surfaces contact occurred well before the load maximum – Frictionless contact had been used. However, it was expected that the friction effect would delay the onset of localization – 3D models should be used
Nielsen et al. [235] - 3D voids collapse and coalescence under intense shearing	Hardening plastic solid	3D cell; contact was modeled by general contact formulation (Abaqus); ALE method with adaptive remeshing	– Changes in initial void size and spacing were shown to have a same effect on the material response and coalescence onset: their decrease led to early coalescence and lower maximum load – Comparison between 2D and 3D models: 2D underestimated both ductility and load carrying capacity. The primary failure mechanisms under shear dominated loadings were similar
Gao et al. [35] - Micromechanical and experimental analyses of stress state effects on ductile fracture	Hardening solid + GTN matrix (2nd population)	3D cell + experiments	– Lode parameter effect was proved via micromechanical simulations – Experiments at different stress states were performed and used to deduce a macroscopic fracture surface

Table 5 (continued)

Authors	Material parameters	Models	Main results
Dunand and Mohr [36] - Lode parameter influence on localization	Hardening plastic solid	3D cell; periodic BCs; general contact formulation; co-rotational (principal stress directions coupled with material rotation) and radial loadings (fixed directions)	– Non-symmetric dependency of E^c upon Lode parameter (ductile fracture was imminent with coalescence onset) – Cut-off value of the stress triaxiality depended on the Lode parameter. For radial loading, this value was lower than that of co-rotational loading – Hosford-Coulomb macroscopic localization criterion was employed, which captured relatively accurate the localization onset

with the Gurson model and validated the conclusion in the [93] study.

The tensile test under hydrostatic pressure can generate a large range of triaxiality values, from negative to highly positive, which is interesting for the study of its influence on damage and fracture of material. Many numerical studies were carried out (such as [67], [131], [130]) to validate these experimental results. However, very high pressure required for this test is its major shortcoming.

Bao and Wierzbicki [59] performed a series of tests including upsetting tests, shear tests and tensile tests on 2024-T351 aluminum alloy to investigate the fracture locus in the equivalent strain and stress triaxiality space ($\overline{\epsilon}$–η space), with a wide range of stress triaxiality values. For each test, the authors determined first the location of fracture initiation and the displacement to fracture, then calculated the evolution of the equivalent strain and stress triaxiality at the fracture initiation location. The strain to fracture was then calculated and represented in the ($\overline{\epsilon}$–η) space to construct the limiting fracture curve. To generate a low stress triaxiality state, new specimens were used in pure shear configurations ($\eta \approx 0$) and combined loading test, while two types of compressive specimens were used to obtain negative stress triaxiality states. The new type of compression test specimen used in [59] helped removing the undesirable effect of friction and the fracture could always be observed on the surface. With the new specimen configuration with different gauge section shapes, one can create a low stress triaxiality involving shear-dominated stress state.

The 2D fracture locus in the ($\overline{\epsilon}$-η) space shown in Fig. 9a revealed that the equivalent strain to fracture varied differently under different stress triaxialities and this dependency was not monotonic, and it drew a lot of attention in ductile fracture community. The results showed the strong dependency of ductility on the stress triaxiality. The shear fracture dominates in the range of negative stress triaxialities while in the range of high stress triaxialities, the fracture occurs due to void nucleation, growth and coalescence. In the transition zone between the above two regimes, fracture might develop as a combination of these two mechanisms. The analytical expressions of the 3 branches of this curve can be found in [59]. However, this result was not confirmed by a recent rigorous study on the same material of [132], which shows a monotonic decrease of the strain to fracture with the stress triaxiality for plane stress loading. More recently, Beese et al. [133] constructed a fracture locus for an aluminum 6061-T6 alloy using series of "uniaxial tests" as well as combined shear-tension tests on the butterfly specimen (see Fig. 8a). The authors observed the same tendency as in [59] (Fig. 9b). However, with the same material, Haltom el al. [134] obtained a different fracture locus by using the combined tension-torsion tests (see Fig. 8b). The strain to fracture monotonically decreased with the increase of the

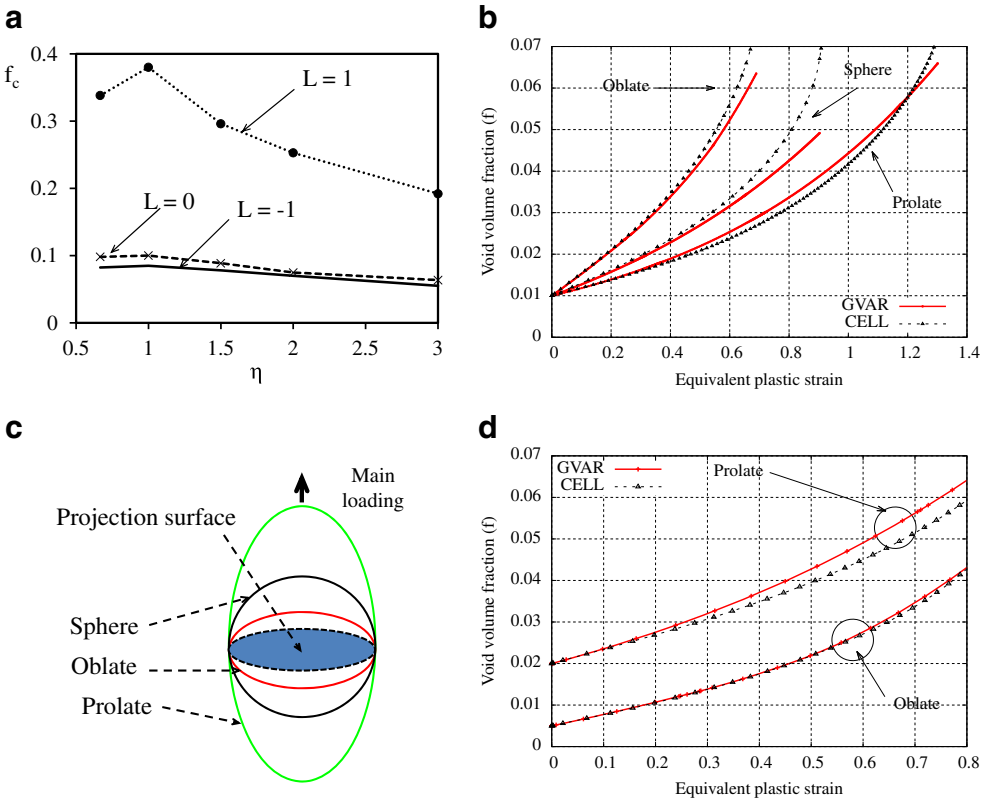

Fig. 7 Illustration of cell computational results **a** the influence of the stress triaxiality and the Lode parameter on the critical porosity (at coalescence); **b** the influence of void shape on porosity evolution ($\eta = 2/3$); **c** different voids with the same projection surface; **d** rate of porosity change for two different void shapes (prolate and oblate) having the same projection area along main loading direction

stress triaxiality (Fig. 9c), which was not materialized by the studies of [59] and [133] (Fig. 9a and b). According to these authors, the difference observed could be explained by the differences in the testing procedures and in the ways the stresses and strains measurements were performed. These authors also indicated that to obtain correct results, the experiments have to respect several characteristics such as: uniform stress in the test section; no stress concentration; no geometric constraints (i.e., the test section must be wide enough for the localization to develop); the deformation must be accurately measured both in uniform regime (relatively large zone) and localized regime (often in narrow zone).

Due to the complexity of loading paths in forming processes (loading paths at different positions of workpiece could be totally different during the processes), the parameters of damage models should be identified and validated for various stress states. Therefore, tests should performed with various values of η and $\overline{\theta}$ - see Fig. 10a from [135] (see also [31, 62, 133, 136, 137]). In addition, these

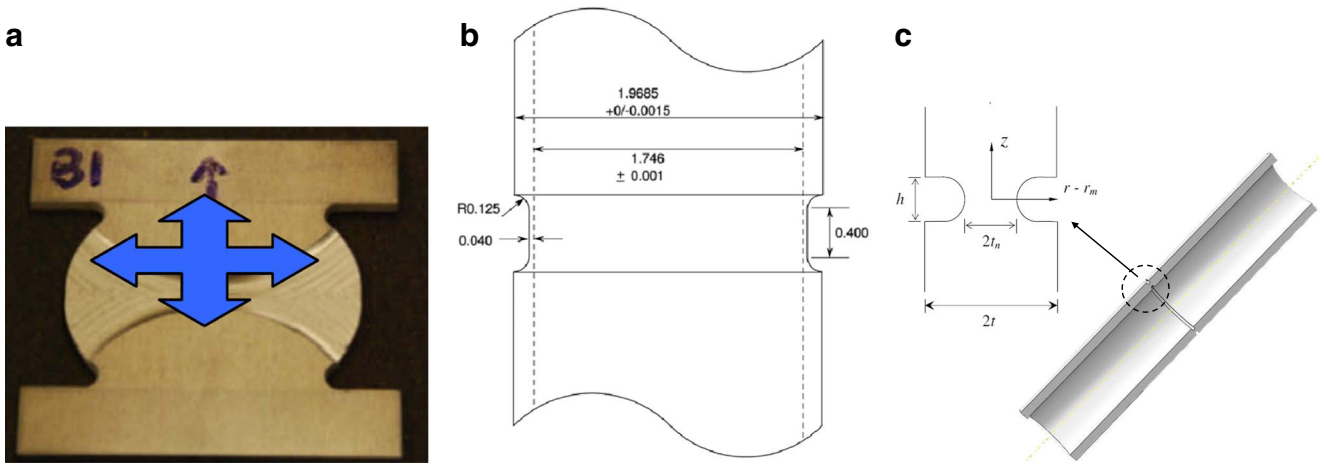

Fig. 8 **a** The butterfly specimen for combined tension-shear tests used in [133]; **b** the tubular specimen for combined tension-torsion test used in [134]; and **c** a half of a tube specimen for combined tension-torsion tests used in [33]

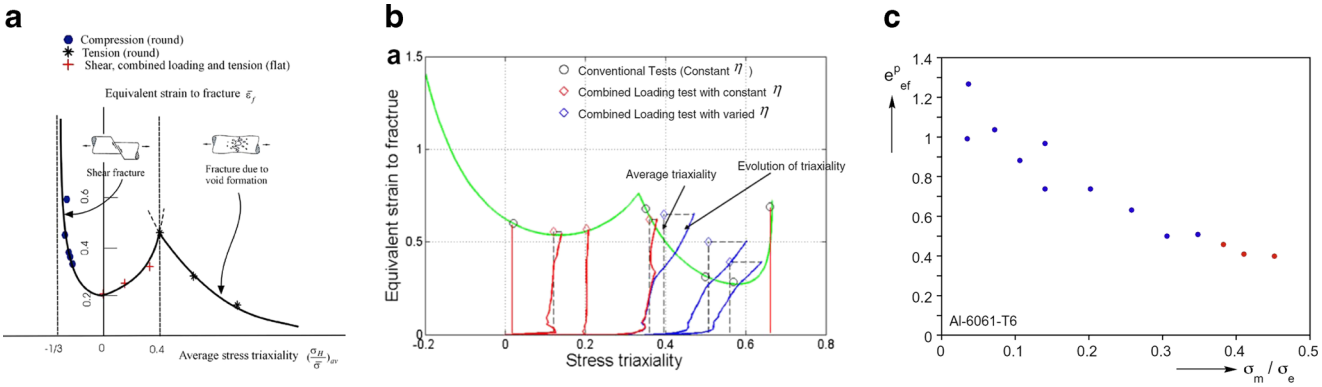

Fig. 9 Dependency of the equivalent strain to fracture on the stress triaxiality: **a** fracture locus for aluminum alloy 2024-T351 obtained from series of conventional tests [59]; **b** fracture locus for aluminum alloy 6061-T6 obtained from conventional tests and combined shear-tension test on butterfly specimen [133] and **c** fracture locus for aluminum alloy 6061-T6 obtained from the combined tension-torsion tests [134]. Figures reprinted from [59], [133] and [134] with permission from Elservier

tests should be performed at same strain-rate and temperature conditions that encountered during the forming process applications. From Fig. 10b, for each value of the stress triaxiality, one can observe the evolution of fracture strain with the Lode angle: the lower the stress triaxiality, the stronger the sensitivity to Lode angle (which is qualitatively in agreement with unit-cell computation results Fig. 2b). Since the stress triaxiality in forming processes is usually weakly positive or negative, accounting for the influence of the Lode angle is indeed necessary.

A series of fracture tests using classical specimens or the butterfly specimen was often carried out to obtain the fracture locus in the $(\overline{\epsilon}–\eta–\overline{\theta})$ space. The butterfly specimen was optimized such that fracture initiated far from the free specimen boundaries [138]. It was used in many recent studies [88, 136, 137, 139]. Many further studies developed this method and the butterfly specimen to establish fracture loci for different materials: cast aluminum alloy ([140]), aluminum alloy 6060-T6 [133], advanced high strength steels (AHSS) [141], using the Modified Mohr-Coulomb (MMC) ductile failure criterion. The butterfly specimen is a very good candidate to carry out fracture tests for a wide range of stress triaxialities. This specimen has several advantages including the same fracture initiation location under different loading combinations. It is also able to remove partly the effect of mesh size (due to the fact that only one finite element model is needed for different loading conditions). However, this specimen has been shown suitable for metal sheet applications (with a special geometry that is not easy to machine) but the applicability to metal wire or bar still needs to be proven. In addition to the butterfly specimen, the double notched tube specimens were also used (see Fig. 8c [33]) to carry out experiments under combined tension-torsion loading. During each test, the load ratio $\kappa = \frac{Nr_m}{M}$ was kept constant (where N, M are axial tension force and torsional loading, r_m is the radius to the center of the notch). The results revealed that the influence of the Lode parameter on void growth and coalescence can be significant. One can generate two different fracture mechanisms with the double notched tube specimen, which can be predicted by the micromechanical models. This specimen might be employed to carry out experiments in low to

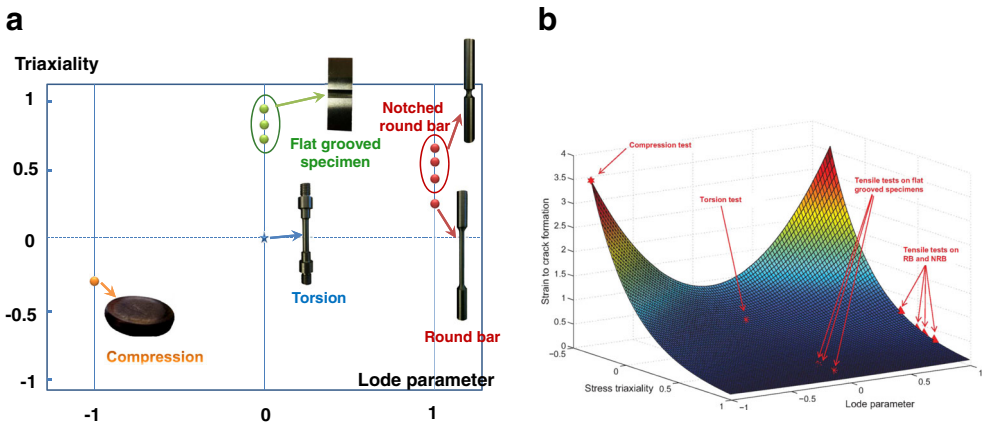

Fig. 10 **a** Conventional mechanical tests in $(\eta, \overline{\theta})$ space, and **b** 3D fracture locus for a high carbon steel ([135])

intermediate triaxiality regime and might be suitable for bar or rod metals. More recently, Papasidero et al. [142] also employed a tubular specimen with a stocky gauge section of uniform thickness to characterize the effect of stress state on the onset of ductile fracture under tension-torsion loading.

In addition to laboratory mechanical tests, tests on processes should also be carried out since they represent the stress states similar to final industrial applications. For several bulk forming processes, additional ultimate wire drawing or drawing followed by tension/torsion/hardness tests could be performed to obtain more reliable parameters both for plasticity and damage models [143, 144] for applications in real industrial process; or half-blanking then wrenching (on a hat-shaped specimen after blanking) tests for industrial applications on a real automotive part (see [145]). Another example is the plane strain compression test on flat specimens, which is often used to characterize the materials for applications in conventional flat rolling process.

A well-constructed damage model can only give correct results for complex applications if its parameters are accurately identified. For complex stress state applications (as in forming processes), damage models should be calibrated from mechanical tests at different loading configurations, covering a large range of stress states. By using these tests, hardening and damage models parameters can be identified and validated for various stress states. In addition, for micromechanics-based models, since they are based on micromechanical considerations, their calibration should be based on both macroscopic tests and microscopic observations ([94, 146–148]). The characterization of each stage of ductile damage requires the continuous monitoring of damage during deformation, which can be done thanks to X-ray tomography measurements [149–152]. However, using a large number of tests leads to laborious calibration tasks, which requires a robust method for optimization procedure.

Models calibration by automatic optimization by inverse analyses

Models calibration could be based on post-processing from strain to fractures of proportional mechanical tests [31, 68, 153] but it suffers a major limitation that only few tests satisfy the proportionality assumption. Automatic optimization by inverse analysis is preferred when a large number of variables and tests is involved. Solving the problem of inverse analysis consists in minimizing a cost function representing the discrepancy between data from a numerical model $\underline{\boldsymbol{F}}$ and data obtained experimentally $\underline{\boldsymbol{F}}^e$ (e.g., the load-displacement curves of tensile tests). For an elasto-plastic model with damage, the mechanical behavior is fully described when all the elastic, plastic and damage parameters are known. The unknowns are the hardening law parameters and the damage model parameters. They define a set of parameters $\mathcal{P}$ that needs to be identified. The parameters identification problem is then expressed as an optimization problem: Find the optimum set of parameters that minimizes the difference between experimental and numerical values. The normalized least square error is chosen as the cost function (ϕ):

$$\begin{cases} \text{Find } \mathcal{P}* \text{ such that} & \phi(\mathcal{P}*) = \min\left(\phi(\mathcal{P})\right) \\ \text{With} & \phi(\mathcal{P}) = \frac{\|\underline{\boldsymbol{F}}^e - \underline{\boldsymbol{F}}(\mathcal{P})\|}{\|\underline{\boldsymbol{F}}^e\|} = \sqrt{\frac{\sum_{i=1}^{N}(F_i^e - F_i(\mathcal{P}))^2}{\sum_{i=1}^{N}(F_i^e)^2}} \end{cases} \tag{34}$$

The cost function can be constructed by using a series of mechanical tests combined with local measurements (with Digital Image Correlation or tomography observations). The process is completed with the choice of optimization method (e.g., an evolution strategy algorithm - [94, 154]). In addition, the inverse analysis computations should be performed in parallel, which will reduce significantly the CPU time.

Discussions on model calibration

Uncoupled phenomenological models

The calibration of fracture criteria is often based on the strain to fracture of a series of test covering a large range of stress states (Section "Experiments for damage study"). Since fracture occurs after large plastic strain, this method requires an accurate characterization of elastic-plastic behavior in order to obtain an accurate value of strain at fracture. It can be done by coupling between macroscopic observation (e.g., load-displacement curves) and local measurement (e.g., strain measurement using DIC or VIC, see [137–139, 155]). Since a high number of data is involved, this method has to be used in combination with automatic optimization programs (Section "Models calibration by automatic optimization by inverse analyses"). Fig. 11a shows an example of the identification of the B&W model's parameters using the displacement to fracture of different mechanical tests presented in Fig. 10a (see [135]).

Coupled phenomenological models

The calibration of coupled phenomenological damage models is often based on the softening effect of damage. This softening, however, depends on the mesh size as shown in numerous studies in the literature (e.g., [156]): a finer mesh leads to a faster damage accumulation. Several methods have been proposed in the literature in order to overcome

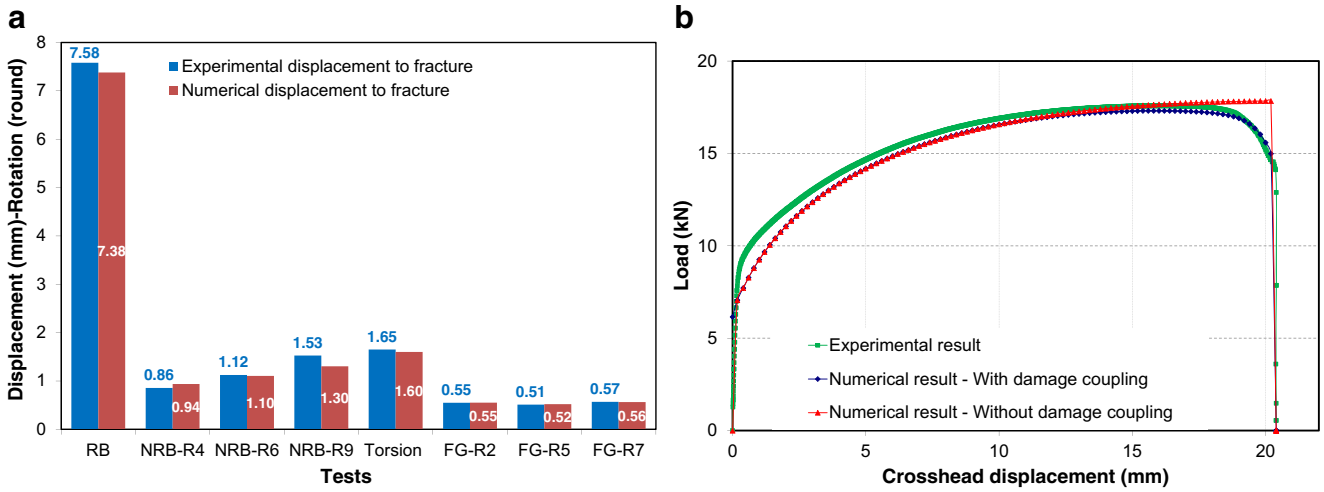

Fig. 11 Calibration of **a** the uncoupled B&W model - based on the comparison between experimental and numerical displacements to fracture of different tests [91]; and **b** the coupled Lemaitre model-based on the comparison between numerical and experimental load-displacement curves of tensile test on RB (the curve with damage coupling takes into account the softening due to damage) [135]

this limitation (e.g., a non-local formulation as used in [157]). If no mesh-regularization technique is employed, the mesh size must be considered as a "material" parameter and damage parameters identified have to be used with the identified mesh size (see the discussion in Section "Mesh size sensitivity"). The identification is often done by inverse analysis using the load-displacement (or stress-strain) curve of a tensile test on round bar [81, 82]. Figure 11b shows an example of the identification of Lemaitre model parameters based on the softening effect of damage for a stainless steel, with numerical results for only elastic-plastic behavior or with damage. As can be observed in Fig. 11b, damage coupling allows modeling accurately the softening of material during the tensile test on RB.

Micromechanics-based models

The calibration of micromechanics-based models needs more attention since it requires micromechanical investigations. Here, the calibration of the widely-used GTN model is discussed. The identification of constitutive parameters q_1 and q_2 could be performed thanks to cell computations (Section "Cell computations") or mechanical tests. However, the nucleation parameters (f_N, ϵ_N, S_N) are often fixed in numerous studies in the literature (although they are strongly material-dependent) since they link directly to microstructural evolution, their measurement is not straightforward. Many authors in the literature carried out the identification of the GTN model parameters on different materials based principally on "macroscopic" mechanical tests. The calibration is often based on tensile tests on notched round bar or compact tension (CT) specimens, where the deformation is localized in the notch area and the stress triaxiality is relatively high. An inverse analysis methodology is often used to identify the parameters (e.g., [158]), based on stress-strain curves (or load-displacement curves).

Recently, new and advanced experimental techniques allow identifying more accurately the values of the GTN model parameters. He and coworkers [159] among others, used in situ tensile tests with scanning electron microscope (SEM) to determine these parameters. This identification was based on the counting of void volume fraction at three damage states. This method gave them relatively exact values of initial void volume fraction as well as void volume fractions at 3 instants of measurement. However, this method could not give a continuous increase of void volume fraction with the plastic strain and could not distinguish the two different damage mechanisms: void nucleation and growth. The characterization of each stage of ductile damage requires the continuous monitoring of damage during deformation, which can be done thanks to X-ray tomography measurements [149–152]. This technique has been used to identify the parameters of the GTN model [146–148]. More recently, Cao et al. [94] combined both mechanical tests and in situ X-ray microtomography observations to identify the parameters of the GTN model. The identified model was then shown to be able to predict accurately both the location and the instant of fracture in a multi-stage wire drawing process. It suggests that, for complex microstructure materials, the identification of damage models should be based on both macroscopic and microscopic observations to obtain reliable parameters. In addition, the model itself must be capable of accounting for the real microstructure parameters associated with the physical problems (e.g., voids for ductile damage phenomenon). It also underlines

the important role of the identification process: a well-constructed damage model can only give correct prediction if its parameters are *accurately* identified.

Numerical modeling of crack growth

Damage to fracture transition

Damage to fracture transition has become a popular topic in the ductile fracture scientific community. Indeed, the transition from a damage continuous approach to a discontinuous fracture is not straightforward both from mechanical and numerical points of view. Continuous numerical modeling of crack growth in initially-uncracked bodies requires a damage model to trigger the onset of micro-cracks. The coupled damage models are often chosen for this purpose since they can capture the continuous degradation due to damage. The use of advanced uncoupled fracture models can describe certain simple crack paths, but they do not take into account the softening effect of damage in a large range of plastic strain before the onset of cracks. In the following, several studies of modeling of crack growth using coupled phenomenological or micromechanics-based models are reviewed.

Tvergaard and Needleman [12] first studied numerically the cup-cone fracture formation based on axisymmetric FE simulation, by using the GTN model [1, 7, 12] and introducing an initial geometrical imperfection. These authors reproduced quite accurately the cup-cone fracture pattern but the use of an initial imperfection was the major limitation of this study. Besson and co-workers [160, 161] used GTN and Rousselier [162] models to study in details the formation of cup-cone and slant fractures as well as the influence of different factors (e.g., mesh design, symmetry, element aspect ratio, constitutive damage parameters etc.) on the numerical fracture surfaces. An indicator was defined by these authors (based on a bifurcation analysis) to detect the zone where strain and damage localization could occur. Based on 2D simulations of plane strain tensile test and axisymmetric tensile test on round bar, the authors concluded that the formation of slant and cup-cone fracture surfaces depends on the constitutive model used as well as mesh size and mesh configuration. The authors showed that, a judicious choice of model constitutive parameters has to be made to obtain the cup-cone fracture (e.g., to obtain this fracture mode, the choice for the critical value of porosity f_c in the GTN model was not a realistic value of the micromechanical parameter).

Despite its simplicity, the element removal technique coupled with remeshing is a convenient way to continuously model the damage to fracture transition for 3D configurations. Mesh dependency may deteriorate the stress field computation at the crack tip, which would be particularly problematic for brittle fracture when the crack path is computed based on stress intensity factor. For ductile fracture, the crack path is less sensitive to the local stress field at the crack tip. Fracture can be driven by ductile damage values and the use of the element erosion with a sufficiently fine mesh may conduct to good crack path prediction. In addition, for large strain applications (e.g., uniaxial compression test or metal forming processes) remeshing approach should be used to avoid extreme element distortions and guarantee well-shaped elements once crack is initiated. The fracture is triggered by critical values of the damage variable and the crack orientation follows the maximum direction of damage. Recently, Cao [163] successfully employed this technique to model cracks growth under different stress states: diagonal crack in compression test, slant crack in tensile test on flat–grooved specimen, cup-cone fracture in tensile test on NRB specimen (Figs. 12, 13 and 14a).

Also with the element removal technique, El Khaoulani and Bouchard [164] used anisotropic mesh adaptation combined with error estimation based on the Lemaitre damage

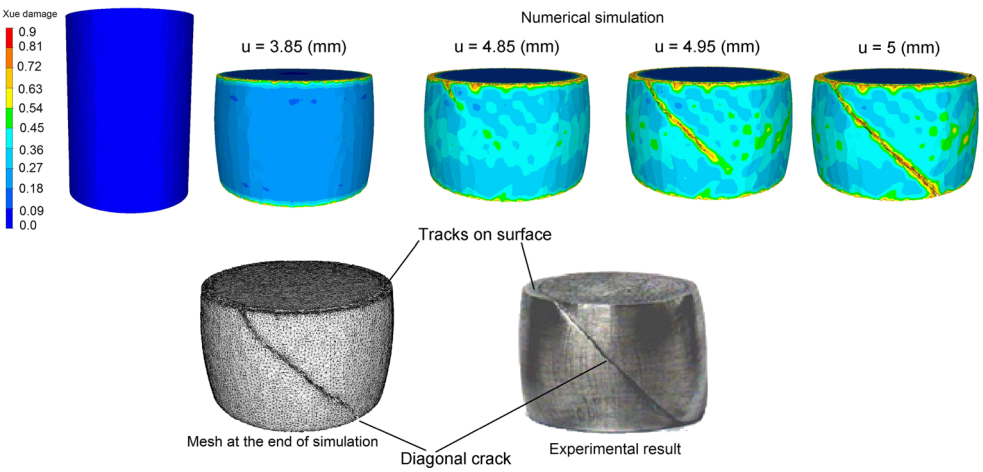

Fig. 12 Comparison between the simulation of crack formation in compression test and the experimental result on the aluminum 2024-T351. Reprinted from [163] with permission from Elservier

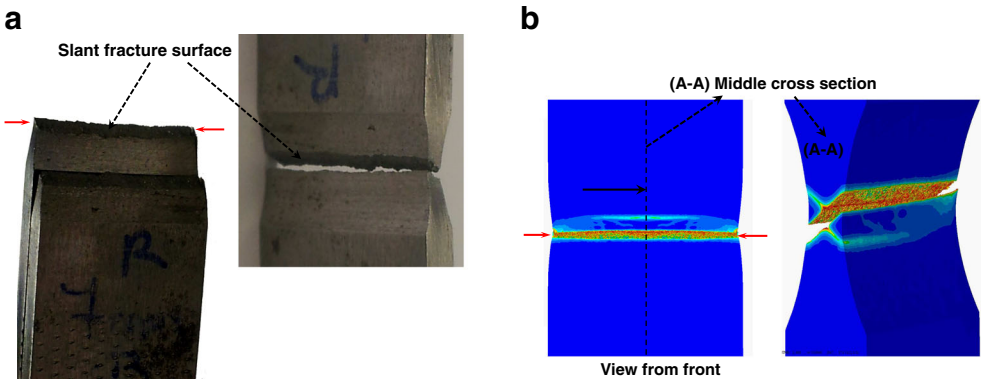

Fig. 13 Comparison between the experimental and numerical fractured surfaces of a flat-grooved pearlitic high carbon steel specimen: **a** experimental slant fractured surface and lateral necking observed; and **b** the left figure shows the lateral "necking" and the right figure shows the view from the middle cross section obtained with numerical simulations [135]

variable and its gradient, to obtain a cup-cone fracture in an axisymmetric tensile test. The main advantage of this method is, starting from a coarse mesh, automatic mesh adaptation and remeshing allow capturing the crack path with sufficient mesh refinement. The CPU time is thus significantly reduced. Mediavilla and coworkers [165, 166] used both coupled (with a regularization technique) and uncoupled damage models combined with a continuous-discontinuous approach as well as a remeshing technique to propagate a crack. More recently, Feld-Payet et al. [167] also employed this technique with a non-local formulation to model crack propagation. These studies required remeshing to insert new discrete crack growth. Cracks were inserted along lines where damage was maximum. Seabra and coworkers [168] proposed a similar continuous-discontinuous approach as in [165, 167] using the XFEM technique [169] and the non local Lemaitre damage model to simulate cracks propagation without remeshing.

The use of micromechanical models (e.g., GTN as in [160]) might also be possible but not with realistic values of the micromechanical parameters. As indicated in [160], the use of the value of their identified critical porosity $f_c = 0.005$ (which defines the onset of coalescence) prohibited the formation of cup-cone fracture. Later, in [161], the authors reported similar results for fracture prediction in plane strain bars under tension. They found that, a judicious choice of $f_c = 0.01$ favored the flat fracture. These results suggest that, even for high stress triaxiality applications, the GTN has some, but not all ingredients to model cup-cone and plane strain fracture (see detailed discussion in [2]). In addition to the choice of a suitable damage models, attention has to be paid to numerical techniques, which are detailed in the following.

The role of numerical technique

As shown in the early work of [12], mesh designs (and mesh size in particular) play an important role in fracture prediction. If no mesh regularization technique is used (e.g., non local model), the results depend strongly on mesh size: a smaller mesh size leads to a higher damage value. The mesh size-dependency also leads to the problem of the dependence of fracture energy on mesh size and this energy can be dismissed if the mesh size tends to infinitely small. The use of non-local models is essential in this case [170], which involves a characteristic length scale that should be

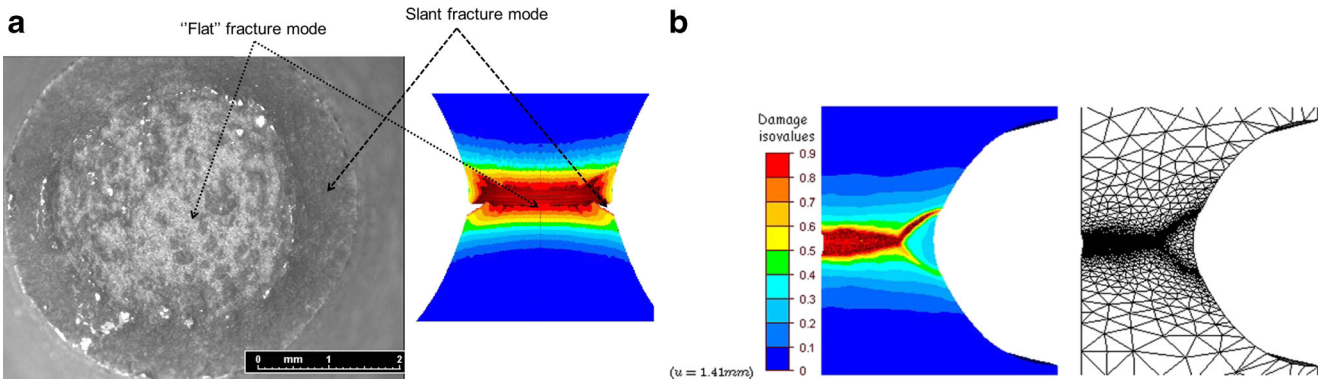

Fig. 14 Cup-cone fracture mode in tensile tests on notched round bar: **a** comparison between experimental result and the numerical result with the Xue model [163] (pearlitic high carbon steel); **b** results obtained with the Lemaitre model and adaptive remeshing (aluminum alloy [164]). For the numerical results, view is from middle vertical cross section. Figures reprinted from [163] and [164] with permission from Elservier

identified from microstructure observation (e.g., void size, particle size, inter-void or inter-particle distances, etc). In addition, in several fracture surfaces (e.g., from a tensile test on notched round bar), one could observe two different void populations: large primary voids with important growth (high stress triaxiality region, e.g., in the center of the bar - flat fracture mode Fig. 14a); and small secondary voids that are nucleated later (in the shear-lip region - slant fracture mode Fig. 14a). For this, it would be necessary to use non local models with two different characteristic length scales associated to two different mechanisms: nucleation and growth to describe crack formation as indicated by Besson and co-workers [3, 170, 171].

Apart from this problem, mesh design is also a crucial factor to describe the crack path. In [12], a zig-zag growth was obtained form tensile test on axisymmetric specimen, which was most likely due to symmetry assumption. In addition, the use of symmetry should be avoided due to resulting non-physical high dissipation energy (see [161]). Elements aspect ratios were shown to have important roles if remeshing was not used. Choosing a suitable initial aspect ratios helps avoiding extreme element distortion when crack is initiated [161]. If remeshing is used to assure well-shaped elements, there is thus no particular attention to be paid on the choice of initial aspect ratios. In [164], the authors used anisotropic mesh adaptation and the Lemaitre model to model the cup-cone fracture. They also reported that without automatic mesh adaptation, a flat fracture mode was obtained instead of a cup-cone mode. Similar results are obtained in [163], in which the author reported that without automatic remeshing, 3D diagonal cracks in upsetting test cannot be captured accurately.

In summarizing, in order to successfully capture cracks formation in ductile solids subjected to complex loadings, the following requirements should be satisfied: (1) the use of a suitable coupled damage model that can capture damage localization for both high and low stress triaxialities; (2) models parameters should be identified from mechanical tests at different loading configurations; and (3) numerical techniques, such as automatic remeshing coupled with accurate remapping, should be used. The main advantage of this approach is the continuous control of damage, from damage accumulation to crack initiation and growth. Neither predefined crack path, nor discrete crack have to be introduced.

Fracture prediction in forming processes

Uncoupled models

Uncoupled models have a major advantage of being easy to implement and use. Since they do not account for the influence of damage on materials behavior, the mesh-dependency due to softening effect of damage is thus avoided. Due to its simplicity, this type of model has been widely used for processes on both flat [172–176] and bulk [91, 144, 177–180] metals. Previous studies employed principally models that account only for the stress triaxiality (e.g., Oyane) or the first princial stress (e.g., Cockcroft-Latham).

Recently-proposed advanced uncoupled models account for both stress triaxiality and Lode dependencies have been used and showed to give satisfied results for complex stress state applications. Li et al. [176] used the MMC fracture criterion to predict fracture limit in the sheet metal forming of ThyssenKrupp TRIP690 steel using four-node shell elements with reduced integration points (S4R in ABAQUS/Explicit). These authors showed that, by using their approach, the crack propagation through thickness due to bending in the punching process, which are not able to be captured by the classical Forming Limit Curve (FLC) approach, can be described. More recently, Liu et al. [181], by comparing different criteria: Johnson-Cook [74], the modified Cockcroft-Latham, the Bao & Wierzbicki empirical [59] and the Bai&Wierzbicki (B&W) models [31] with consideration of rate dependency and temperature effect, showed that the modified B&W can accurately describe the chip removal behavior of materials (2D finite element model under plane strain deformation was used with quadrilateral continuum element CPE4RT in Abaqus/Explicit). Cao et al. [91, 135, 144, 182] employed the B&W and MMC models (with the tetrahedral finite elements P1+/P1) to predict fracture in bulk forming processes, involving multi-stage drawing, wire rolling and cold pilgering. The simplified Xue and Wierzbicki fracture criterion, whose parameters were identified from both conventional tensile tests and half-blanking then wrenching laboratory tests (loading is close to the real industrial process), was also successful applied to model the fracture during operating of an automotive part [137] (see Fig. 15).

Although the uncoupled models have been successfully applied to predict damage and fracture in different forming processes for both flat and bulk metals, the major shortcoming of these models is that they does not account for the softening effect due to damage accumulation. In addition, for complex stress state and non-proportional loadings, the damage parameter does not has a physical interpretation. Due to their phenomenological grounds, special care should be taken for their application outside the identification domain.

Coupled phenomenological models

Among coupled models proposed in the literature, the Lemaitre-like models seem the most used to predict fracture

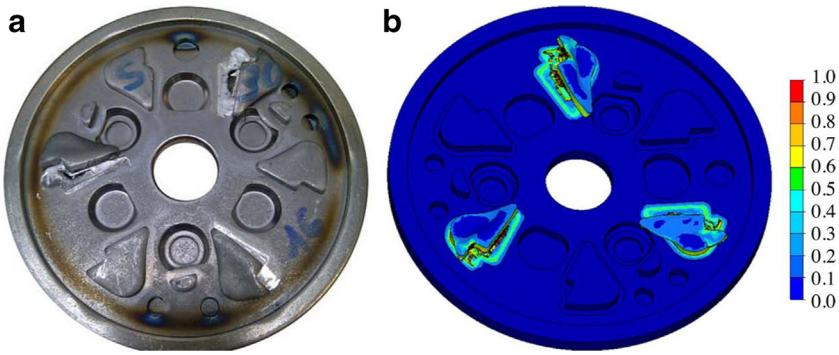

Fig. 15 **a** Experimental wrenched fixed flange and **b** simulation wrenched fixed flange using the simplified Xue and Wierzbicki fracture criterion ([137]). The investigated material was a high-strength low-alloy steel S420MC, and the tetrahedral finite elements P1+/P1 were used for numerical simulations. Figures reprinted from [137] with permission from Elservier

in forming processes. A comprehensive review of the CDM framework for metal forming simulations was given by Saanouni and co-workers [87, 183]. This kind of model has been shown adapted for processes that involve high stress triaxiality ([86, 89, 143, 183]).

Figure 16 shows the comparison between cracks observed at the outlet in wire round rolling process from experiment (Fig. 16a) and from numerical prediction with the Lemaitre-type model (Fig. 16b). For this process, fracture occurs on the wire surface. It should be noted that, in [135, 144], the authors showed that the Lemaitre-type models give correct prediction for both fracture location and the instant of fracture for this process[11].

Figure 17 shows another application with the Lemaitre-type model (from [86, 184]) for the extrusion process. In such a process, chevron cracks are often observed in the center of metal wires, which are shown on the left of Fig. 17. The stress state at this position can be approximated by a uniaxial tension (in the extrusion direction) superimposed to certain hydrostatic pressure (due to die); and the stress triaxiality is positive. Predicted results obtained with the Lemaitre model (with the kill element technique) show a good agreement with experimental observations.

However, for processes involving important shear effect, the Lemaitre-type model sometimes cannot provide a good prediction of damage localization [89, 91, 135]. Recently, by comparing with the modified coupled Xue model [185], Cao et al. [89] showed that the Xue model, with Lode-dependency, provided accurate damage localization for a wire flat rolling process (parameters of both models were identified from different conventional mechanical tests on a high carbon steel). Based on this result, the modified Lemaitre model accounting for Lode-dependency proposed by [88] was adopted and provided similar results in terms of damage localization prediction as the phenomenological Xue model [91].

[11]These authors also showed that the B&W model also provided correct results for the round wire rolling process.

Micromechanics-based models

Compared to other models, micromechanics based models are not often used in the simulation of industrial forming processes. The reason could be due to their complexity, the cost that must be spent in terms of CPU time and also their limitation for complex stress states. Furthermore, their calibration needs continuous following of microstructure or micromechanical computations (see Section "Microme-chanics-based models") to obtain realistic parameters. In addition, since the Gurson framework has a major shortcoming in fracture prediction at low stress triaxiality and shear-dominated loadings, its usage seems limited for bulk forming processes with moderate values of the stress triaxiality (e.g., [91, 135, 186, 187] for the wire drawing; [91, 135] for the wire flat rolling process).

Cao et al. [91, 135] compared different model in three approaches of ductile damage for fracture prediction in wire drawing and wire flat rolling processes. Figure 18 shows the predictive damage maps obtained with six different models for the second pass of wire drawing.

Figure 18 shows that, except the modified GTN model by Xue[12], all other models provided correct results of maximum damage location: in the wire center (as observed in experiments). These authors then investigated damage evolution at the wire center (the critical position) obtained with the five models in order to determine the instant of fracture predicted by these models for the whole 14-pass process (i.e., the instant that the damage parameters reach their critical values) - see Fig. 19.

As can be observed, for all phenomenological models used (B&W, Xue, Lemaitre, LEL), although they provided a good prediction of maximum damage location, they failed to predict the instant of fracture: fracture was predicted after 4 passes with the B&W model; after 5 passes with Xue, Lemaitre and LEL models (in experiments, fracture occurred after 14 passes). Only the GTN model, which

[12]See [188] for the details on the implementation of the Gurson model in a FE element code (Forge®) dedicated to forming processes simulation based on a mixed velocity-pressure FE formulation.

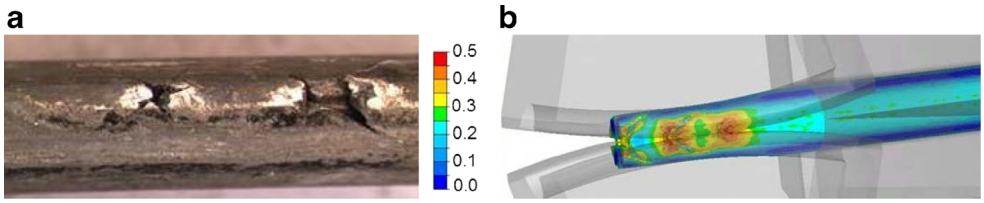

Fig. 16 **a** Experimental observations of cracks on the surface of rolled wire; **b** numerical prediction obtained with the Lemaitre-type model, showing cracks at outlet [135]

was calibrated from both mechanical tests and tomography observations [94] gave a comparable result in this case: fracture was predicted after 13 passes. However, for another application in wire flat rolling, the GTN model could not provide a correct prediction of maximum damage location in sheared regions [91, 135]. It was due to the fact that the original GTN model does not account for the "shear" influence (voids remain spherical during pure shearing without any void growth).

Discussions

The choice of damage model

A good predictive model involves a tradeoff between its simplicity and its prediction quality. For the simplicity, the physics must be simplified as much as possible and only the key dominant factor remains. If the predictions are good, it means that not only a reliable predictive tool is obtained, but also that the underlying physical assumptions are correct and that the physics phenomenon is well captured. Sometimes the physics is too complicated and no physical model is available. A phenomenological model is then fully justified, even though it will not deliver much insight on the physics. The uncoupled model has a major advantage of being easy to implement and use. In addition, since no coupling is taken into account (i.e., no softening due to damage), there is negligible influence of mesh size. However, this model suffers from several limitations, mainly its purely phenomenological nature (i.e., no physical parameters involved). Phenomenological coupled damage models also suffer the same limitation because of their phenomenological grounds, although these models account for the softening due to damage. This softening effect is sometimes important, especially at very large strain encountered in multi-stage forming processes (i.e., in the last stages of damage, just before failure). In addition, the Lemaitre-family models are derived within the framework of continuum damage mechanics, which ensures the thermodynamic consistency[13] (although this property is not enough for a material model to be accurate and predictive). From a strict micromechanics viewpoint, in these models, the evolution of damage variable does not link with a microstructure change (e.g., the evolution of voids in material). If voids grow, the total volume of material must change (maybe very small) since the matrix is incompressible, this cannot be captured by the use of these phenomenological models.

Regarding micromechanical approach, although the Gurson and GTN model are linked with micromechanical considerations, they are still based on an ideal representation of voids: they are spherical and keep their shapes during the deformation process. For forming processes, e.g., wire drawing and rolling, voids are elongated in the drawing direction in the wire drawing process and voids are flattened and rotated following the shear band in the rolling process. Furthermore, this approach still suffers some limitations: the nucleation and coalescence laws are purely phenomenological (GTN model), the yield function violates the upper bound proposed by [118] at low stress triaxiality (Gurson model). The GTN model has an advantage of being simple enough for implementation in standard FE codes (and has been widely used in ductile damage community). The damage parameter is linked with the void volume fraction and volume change by void growth can be described. However, the nucleation and coalescence laws

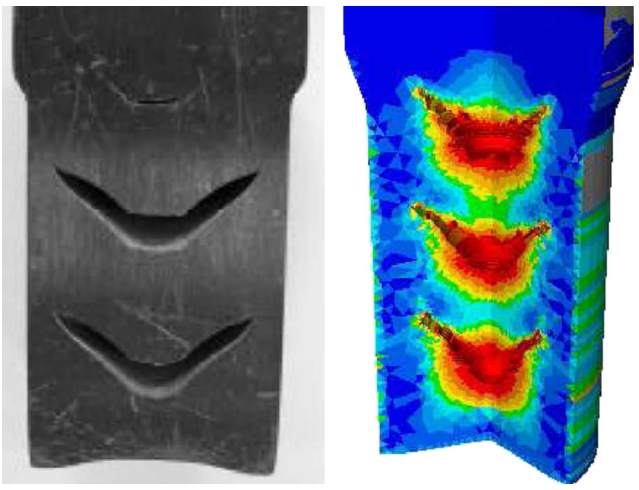

Fig. 17 Chevron fractures observed in experiment (*left*) and predicted by the Lemaitre-type model (*right*) during the extrusion process [86, 184]

[13] For the original GTN model, the thermodynamic consistency can also be demonstrated provided that the void nucleation is absent (as already shown in [3, 24]). A thermodynamic extension of the existing local Gurson-based model was presented in Reusch et al. [189].

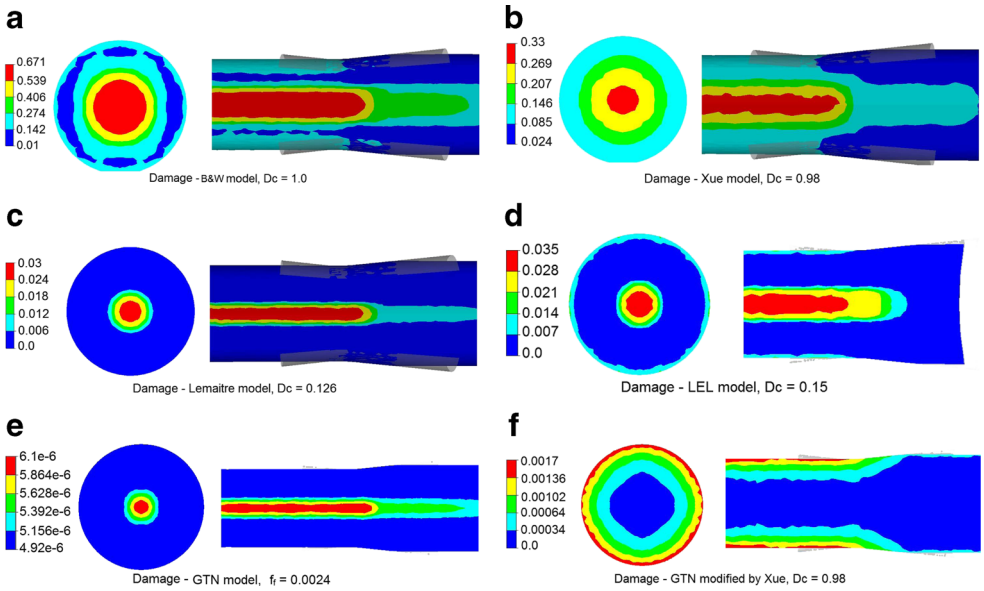

Fig. 18 Damage at steady state of second drawing pass for six damage models: **a** Bai & Wierzbicki [31], **b** Xue [185], **c** Lemaitre [81], **d** LEL [88], **e** GTN [7, 12] and **f** modified GTN by Xue [30]. The values are represented on the longitudinal and transverse cross sections (figure adapted from [91])

should be enhanced by using more physical inspired formulations, such as the nucleation law proposed by Bouaziz, Maire and their coworkers [95, 150]; Thomason or Brown and Emburry criteria for coalescence [54]. In addition, void growth is also influenced both by material's microstructure (particles, elongated grains with heterogeneous phases, etc.) and forming processes itself (e.g., elongated voids are observed in drawing direction). The GLD-like models with the latest extension by Madou and Leblond [190], although take into account the ellipsoidal void shape, still do not account for the rotation of voids. In addition, their high number of parameters make them too costly for applications in industrial forming processes. The use of a micromechanical model, which accounts for void shape change and void rotation, is of great interest. The GVAR [117] and SOM [115, 116] models consider general ellipsoidal voids embedded in an elastoplastic matrix subjected to 3D deformation, and the evolution of the void volume fraction, aspect ratios and orientations can be described. In addition, loading is not necessarily aligned with voids axes. These two models have been shown to give correct results for various loadings and void shapes. However, the SOM model is currently computationally inefficient. The application of the GVAR model to complex applications such as multi-stage forming processes is thus of prime interest. However, the description of voids in all these micromechanics-based models remains idealized in the sense that it does not account for particles fragmentation and real forms of voids. In that sense, these models have clearly more physical bases than the phenomenological approaches, but they are still based on an idealized representation of voids and different underlying assumptions that have not been clarified. In addition, since coupled models (phenomenological or micromechanics-based models) involve damage softening, the results of damage depend strongly on the mesh size. This problem can be treated by considering the mesh size as a parameter (lack of physical underlying) or using a non-local model (costly).

In this context, the use of "modular" models is promoted [91, 135]. The idea is, regarding its physical origin, a given damage model can be enhanced by adding suitable "ingredients" (e.g., a Lode-dependent term, or a strain threshold for damage accumulation that depends on the stress triaxiality) to improve its prediction ability. If all the ingredients are well-constructed, different models may converge to a same prediction in terms of damage localization (as shown in [91, 135] for the wire flat rolling process). Several examples can be taken to illustrate this idea: the B&W model is obtained from the well-known Rice and Tracey formulation for fracture at high triaxiality, by introducing (phenomenologically) a quadratic dependency of strain to fracture to the Lode parameter; the modified

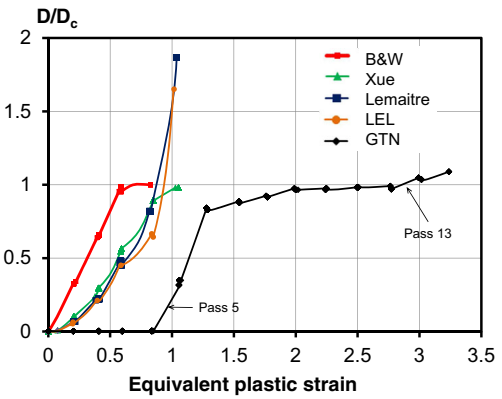

Fig. 19 The evolution of normalized damage parameters (normalized by their critical values) during the multi-stage wire drawing process. Each pass is represented by the line between two symbols

GTN model for shear loading is obtained by adding a Lode-dependent term to the evolution of the void volume fraction; or the LEL model is obtained from the Lemaitre model by adding a parabolic Lode dependent term. It should be noted that, with this kind of approach, all models become phenomenological. To the best of the present author's knowledge, no purely micromechanical model has been shown to be capable of capturing both damage mechanisms at high and low stress triaxiality in real multi-stage shear-dominated manufacturing processes (due to their construction and also their current computational inefficiency). For the moment, the use of phenomenological modular models might be fully justified if they can provide correct predictive results.

Several recent studies are seeking to model real microstructure in a Representative Elementary Volume during deformation. The mesh of this real microstructure and realistic boundary conditions obtaining from tomography/laminography images coupled with the volumetric digital image correlation technique allow modeling and understanding ductile mechanisms in complex loading paths. Examples of modeling of these mechanisms are presented in [191–193] and offer new opportunities to better understand the influence of microstructure (inclusion) and loading path on void nucleation and coalescence mechanisms.

Mesh size sensitivity

Mesh dependency due to softening by damage growth has been reported in numerous studies in the literature. The problem with local behavior of a softening model is that when a material point starts to soften, it takes up most deformation leading to intense damage growth and resulting in further softening at that point. In FE simulations, after localization, the deformation accumulates in one element (or a row of elements). An infinitely small mesh would result in approximately no energy dissipation in the localization band and diminishing the mesh size does not lead to converged results [3]. In mathematical point of view, the local material model results in the loss of ellipticity of the boundary value problem in statics. The mathematical problem then becomes ill-posed, leading to the dependence of the results on the direction and size of the FE mesh [194]. To solve the mesh dependency problem, many methods, namely regularization methods, have been proposed: using enhanced theories that account for spacial derivatives of displacement fields [3, 195, 196]; using viscoplastic regularization (e.g., [197]); or using non-local models [198, 199]. The enhanced-theories introduce additional degrees of freedom (DOF) to describe the deformation and rotation of a microstructure, in which the most general case is the micromorphic theory with nine additional DOF for micro-deformation and micro-rotation [196, 200, 201]. For the case of ductile damage induced by void growth, a micro-dilatation theory was derived within this framework [202] but its use was restricted to models where damage is controlled by volumetric variation. Regarding the viscoplastic regularization, when the deformation rate starts to increase in the soft element (i.e., damaged element), the increase of strain rate makes the element stiffer, which prohibits the deformation to accumulate in that element. This approach has been principally used for dynamic problems [203–205] since there is no explicit expression derived for the viscoplastic length scale for static problems. For this reason, the non-local models are often used to treat the mesh dependency due to damage induced softening. These models consider that the behavior of a given material point does not only depend on the local values of state variables, but also on the values of one or several variables in a domain around this point, whose size is defined by a materials characteristic length independently on any mesh size. There are two main strategies that allow to compute the non-local variable: (1) through an integral type function [206]; and (2) through gradient-based equations [157, 207]. These two approaches have been shown equivalent, but the latter one is simpler to implement since the non local variable can be defined as nodal variables in the FE framework [3]. Details on non-local models can be found in [3, 198, 199] and are not recalled here.

For practical applications, especially for real-scale FE simulations of forming processes, non-local models have not been often used due to computational cost in terms of CPU time. Indeed, regardless of non-local methods, a characteristic length scale, which is an intrinsic parameter of the material, has to be defined and the mesh size must be smaller than this length. For metallic materials, the choice of this length is still a subject of numerous debates (it could be considered as the average size of inclusions or the average distance between two inclusions or defects, etc.). Besson [3, 170, 171] also suggested that, it would be necessary to employ two characteristic length scales in order to capture two mechanisms (growth and nucleation) of ductile damage. In addition, since the characteristic length is in the order of ten to hundred micrometers, the chosen mesh size is thus very small leading to a huge DOF for real scale model FE simulations. For this reason, for industrial forming applications, the mesh size is often fixed, and the damage and plasticity models parameters have to be identified from mechanical tests whose FE models employ the comparable mesh size as in forming applications [91, 144, 182]. This strategy would help reducing partly the influence of the mesh size.

Rate and temperature dependencies

Forming processes involve multi-physical problems. Even for "cold" condition, the friction between tools and workpiece and the heat due to plastic deformation increases the temperature of the workpiece. The temperature should be taken into account, both for elasto-plastic constitutive equations and damage models. In addition, several processes are performed at high velocity (e.g., the drawing speed can be up to 20 ms^{-1}, leading to very high strain rate). Accounting for such influences would be of great interest for certain materials. In the present review, the strain-rate and temperature effects are not accounted in damage models. They would be easily incorporated in modular models by adding, e.g., accurately-constructed strain-rate and temperature dependent terms. Johnson and Cook [74] showed that the ductility of different materials (OFHC copper, 4340 steel and ARMCO iron) increases with the strain rate. Later, based on their cell computations, Brocks et al. [122] also found that the void volume at coalescence onset (f_c) increases with strain-rate and decreases with temperature but these impacts are negligible. The increase of ductility with strain-rate was also reported in recent studies of Erice et al. [208] for martensitic stainless steel FV535, Khan and Liu [209] for aluminum 2024-T351, Roth and Mohr [210] for DP590 and TRIP780 steel grades. However, for micromechanics-based models, the problem is more complicated since these dependencies should be accounted from micromechanical investigations and the derived models have to remain simple enough for real-scale metal forming applications.

Anisotropy

Anisotropy of material matrix (due to material processing) and morphological anisotropy (initial non-spherical particles, or induced by void shape) have been shown to have important effects on ductile fracture. A non-associated anisotropic fracture model was proposed for aluminum 6260-T6 based on the MMC model and scalar anisotropic plastic strain measure is defined through the linear transformation of the plastic strain vector [139]. In the CDM approach, damage anisotropy can be described though a damage tensor instead of a scalar as in isotropic models. The complexity of the model depends on the order of the damage tensor: first order (see, e.g., [211]), second order [212–217], or higher order ones (e.g., [218–220]). In theory, the use of high order damage tensor should provide more accurate prediction on the damage evolution. However, the high numbers of material constants as well as the inefficiency of numerical algorithm have limited their applications in complex industrial forming applications. The Gurson-like model has also been improved to incorporate the anisotropy of material's matrix (e.g., [26–28]). However, the void shape-induced anisotropy cannot be captured by using these models as well as phenomenological models mentioned in this paragraph. Monchiet et al. [221] proposed a homogenization-based macroscopic yield function that combines both orthotropic matrix and void shape effects, which was further improved by Keralavarma and Benzerga [128, 222] who considered richer deformation fields at the microlevel. These models remain complicated and have not been validated for general three dimensional complex loadings that involve both void volume and shape change and void rotation. The use of recent sufficiently simple models (VAR and GVAR) that have been validated for real scale FE applications would be of interest when combined with Hill [223], Barlat [224], or Bron&Besson [225] anisotropic matrix to describe both anisotropies.

Kinematic hardening

The kinematic hardening is of great importance when loading is nearly cyclic (e.g, in the pilgering process - see [135, 226]). In addition, as indicated in [3], comparisons of FE computations using either isotropic or kinematic hardening and constant damage parameters revealed that kinematic hardening could accelerate the occurrence of failure. For the processes presented in this review, loadings are not cyclic and thus the kinematic hardening has been neglected. However, it is straightforward to introduce the kinematic hardening using phenomenological models. For micromechanical models (Gurson framework), as also indicated in the paper, several extensions for kinematic hardening have been proposed in the literature [23–25]. Accounting for this effect could be important to describe the effect of restraining on material ductility (e.g., [227]).

The cutoff value of the stress triaxiality

The cutoff value of the stress triaxiality of -1/3, below which fracture does not occur, has been often chosen as proposed in [228] (see [86, 229, 230]). Bao and Wierzbicki [228] analyzed the tests under pressure of Bridgman [129] to deduce this value. It should be noted that, the tests performed by Bridgman used principally axisymmetric specimens (bulk material). However, Lou et al. [77] showed that this value is far from universal, and these authors proposed a changeable cutoff value. Although it was based on phenomenological grounds, this study revealed that the choice for the cutoff value of stress triaxiality is still an open question. For forming processes, this choice is of great important since

the stress triaxiality in numerous forming process is often negative or just slightly positive. In [185], the author investigated the fracture locus (the strain to fracture as a function of the stress triaxiality) for plane stress state for the same Aluminum alloy 2024-T351 as in [59] and [77]. The author reported a cutoff value approximated -2/3 instead of -1/3 used by [59] (see Fig. 5 of [185]). In their comparative studies, Cao et al. [91] compared the results of damage localization obtained with the cutoff value of -1/3 [228] and -2/3 [185]. These authors showed that the choice of the cutoff value has a strong influence on damage localization in wire flat rolling process but it has negligible influence on the drawing process. This reveals the strong influence of this value, and its identification is still an open question.

Closure remarks

The development of ductile damage models have been continuously progressed in the last decades. While the reviews on porous plasticity framework and continuum models were given in the literature [1–3], the present review focuses on practical considerations and the comparison between these two approaches and the uncoupled approach (which is often preferred in industrial applications). Indeed, reliable predictive results can be obtained with uncoupled phenomenological models if they are well-constructed and models are correctly calibrated. However, since these models and coupled phenomenological models are based on phenomenological grounds, the applications outside the identification zone require special attention. Regarding Gurson-like approach, its developments and applications have been the subject of numerous studies in the literature. However, the Gurson-like model is well-known suffered from several limitations (Section "Gurson-like limit analysis kinematic approach"), and attempts to overcome these shortcomings make the model become phenomenological. Several three-dimensional models incorporating void shape change and void rotation have been developed within an alternative micromechanical framework, based on nonlinear homogenization method [109, 111–117]. This class of models allows better capturing different features of microstructure, instead of only the volume change (as in Gurson framework) or eventually void shape change in a more complicated GLD framework (which, in practical consideration, is computationally expensive for industrial forming applications). However, since the initial model (VAR) suffers from the limitation at high triaxiality, its modification (MVAR) in contrast, leads to high compliant yield surfaces. Moreover, the SOM model, even very accurate, is currently computationally inefficient. The latest development by [117] based on *ad-hoc* modifications of the original VAR model within this framework, and in the same time keeping the functional form of Gurson model, reveals the efficiency of the new proposed model for real-scale model simulation. Further applications to metal forming process would be of interest.

The review does not consider a class of numerical methods for ductile fracture and localization-linked-failure modeling, such as enhanced and mixed finite element methods [169, 231], cohesive-zone model [123], or non-local formulations [156, 199]. In addition, developments of physically-based thermal-(visco)-plasticity models are not mentioned as well. These models are believed allowing to obtain more accurate results but are currently computationally inefficient for manufacturing processes. Moreover, as also indicated in the text, for reliable results for complex stress states, models have to be calibrated from mechanical tests as well as microstructure observations, with a robust automatic optimization procedure. The efforts put into improving all these aspects and the development of new models will open the door for extensive applications in metal forming processes.

Acknowledgments The author would like to acknowledge Pierre-Olivier Bouchard and Pierre Montmitonnet at the Center for Material Forming for fruitful discussions. Special thank is due to Jacques Besson at the Centre des Matériaux, Mines Paristech for the advices and the helpful discussions regarding numerical aspects.

References

1. Tvergaard V (1989). Elsevier, pp 83–151
2. Benzerga AA, Leblond JB (2010). In: Advances in Applied Mechanics, vol 44. Elsevier, pp 169–305
3. Besson J (2010) Int J Damage Mech 19(1):3
4. McClintock FA, Kaplan SM, Berg CA (1966) Int J Fract 2:614
5. McClintock FA, ASME J (1968) Appl. Mech 35:363
6. Rice JR, Tracey DA (1969) J Mech Phys Solids 17:201
7. Gurson AL (1977) J Eng Mater Technol 99(1):2
8. Tvergaard V (1981) Int J Fract 17:389
9. Chu CC, Needleman A (1980) J Eng Mater Technol 102(3):249
10. Dalloz A, Besson J, Gourgues-Lorenzon AF, Sturel T, Pineau A (2009) Eng Fract Mech 76(10):1411
11. Needleman A, Tvergaard V (1984) J Mech Phys Solids 32(6):461
12. Tvergaard V, Needleman A (1984) Acta Metall 32(1):157
13. Thomason P (1985) Acta Metall 33(6):1087
14. Thomason P (1985) Acta Metall. 33(6):1079
15. Pardoen T (2000) Hutchinson, J.W. J Mech Phys Solids 48(12):2467
16. Benzerga AA (2002) J Mech Phys Solids 50(6):1331
17. Scheyvaerts F, Onck P, Tekoglu C, Pardoen T (2011) J Mech Phys Solids 59(2):373
18. Benzerga AA, Leblond JB (2014) J Appl Mech 81(3):031009
19. Gologanu M, Leblond JB, Devaux J (1993) J Mech Phys Solids 41(11):1723
20. Wen J, Huang Y, Hwang KC, Liu C, Li M (2005) Int J Plast 21(2):381
21. Monchiet V, Bonnet G (2013) Int J Solids Struct 50(2):320
22. Siruguet K, Leblond JB (2004) Int J Plast 20(2):225
23. Leblond JB, Perrin G, Devaux J (1995) European journal of mechanics and Solids 14(4):499
24. Besson J, Guillemer-Neel C (2003) Mech Mater 35(1-2):1
25. Mühlich U, Brocks W (2003) Comput Mech 31:479

26. Benzerga AA, Besson J, Pineau A, Eng J (1999) Mater Technol 121(2):221
27. Benzerga AA, Besson J (2001) Eur J Mech A Solids 20(3):397
28. Benzerga AA, Besson J, Pineau A (2004) Acta Mater 52(15):4639
29. Nahshon K, Hutchinson JW (2008) Eur J Mech A Solids 27(1):1
30. Xue L (2008) Eng Fract Mech 75(11):3343
31. Bai Y, Wierzbicki T (2008) Int J Plast 24(6):1071
32. Xue L, Wierzbicki T (2009) Int J Solids Struct 46(6):1423
33. Barsoum I, Faleskog J (2007) Int J Solids Struct 44(6):1768
34. Barsoum I, Faleskog J (2011) Int J Solids Struct 48(6):925
35. Gao X, Zhang G, Charles R (2010) Int J Damage Mech 19(1):75
36. Dunand M, Mohr D (2014) J Mech Phys Solids 66(0):133
37. Gurland J, Plateau J (1963) Trans ASM 56:442
38. Goods SH, Brown LM (1979) Acta Metall 27(1):1
39. Argon AS, Im J, Safoglu R (1975) Metall Trans A 6:825
40. Beremin FM (1981) Metall Trans A 12:723
41. Eshelby JD (1957). In: Proceedings of the Royal Society of London, vol 241, p 376
42. Berveiller M, Zaoui A (1978) J Mech Phys Solids 26(5-6):325
43. Benzerga AA Rupture ductile des tôles anisotropes. Ph.D. thesis, Ecole nationale supérieure des Mines de Paris. 2000. French
44. Lee BJ, Mear ME (1999) J Mech Phys Solids 47(6):1301
45. Lee BJ, Mear ME (1999) Mech Mater 31(1):9
46. Needleman A, Rice JC (1978) Mechanics of sheet metal forming:237–267
47. Zhang ZL, Thaulow C, Ødegard J (2000) Eng Fract Mech 67(2):155
48. Huang Y (1991) J Appl Mech 58(4):1084
49. Thomason PF (1990) Ductile Fracture of Metals. Pergamon Press, Oxford
50. Tvergaard V (1998) Int J Solids Struct 35(30):3989
51. Pardoen T, Scheyvaerts F, Simar A, Tekoglu C, Onck PR (2010) Comptes Rendus Physique 11(3-4):326
52. Weck A, Wilkinson DS (2008) Acta Mater 56(8):1774
53. Weck A (2007) The role of coalescence on ductile fracture. Ph.D. thesis, McMaster University
54. L.M. Brown, J.D. Emburry (1973). In: Proceeding of 3rd International conference on the Strength of Metals and Alloys, Cambridge
55. Thomason PF (1968) J Inst Met 96:360
56. Fritzen F, Forest S, Bòhlke T, Kondo D, Kanit T (2012) Int J Plast 29(0):102
57. Khdir YK, Kanit T, Zaïri F, Naït-Abdelaziz M (2015) Eur J Mech A Solids 49(0):137–145
58. Landron C (2011) Ductile damage characterization in Dual-Phase steels using X-ray tomography. Ph.D. thesis, L'Institut National des Sciences Appliquées de Lyon
59. Bao Y, Wierzbicki T (2004) Int J Mech Sci 46(1):81
60. Zapara M, Tutyshkin N, Müller WH (2013) Key Eng Mater 1125:554–557
61. Tutyshkin N, Müller WH, Wille R, Zapara M (2014) Int J Plast 59(0):133
62. Cao TS, Gaillac A, Montmitonnet P, Bouchard PO (2013) Int J Solids Struct 50(24):3984
63. Kweon SS, Beaudoin AJ, McDonald RJ (2010) J Eng Mater Technol 132(3)
64. Kweon S (2012) Eur J Mech A Solids 31(1):203
65. Achouri M, Germain G, Santo PD, Saidane D (2013) Materials & Design 50(0):207
66. Budiansky B, Hutchinson JW, Slutsky S (1982) The Rodney Hill 60th anniversary volume:13–34
67. Bao Y, Wierzbicki T (2004) J Eng Mater Technol 126(3):314
68. Bai Y, Wierzbicki T (2010) Int J Fract 161(1):1
69. Lou Y, Huh H, Lim S, Pack K (2012) Int J Solids Struct 49(25):3605
70. Lou Y, Huh H (2013) Int J Solids Struct 50(2):447
71. Lou Y, Huh H (2013) J Mater Process Technol 213(8):1284
72. Cockcroft M, Latham DJ (1968) Ductility and workability of metals, vol 96. 1 Carlton House Terrace, England
73. Wilkins ML, Streit RD, Reaugh JE (1980) Technical report UCRL-53058. Lawrence Livermore National Laboratory
74. Johnson GR, Cook WH (1985) Eng Fract Mech 21(1):31
75. Xue L (2007) Duct ile fracture modeling - Theory, experimental investigation and numerical verification. Ph.D. thesis. Massachusetts Institute of Technology (MIT)
76. Gruben G, Hopperstad O, Borvik T (2012) Int J Mech Sci 62(1):133
77. Lou Y, Yoon JW, Huh H (2014) Int J Plast 54(0):56
78. Benzerga AA, Surovik D, Keralavarma SM (2012) Int J Plast 37(0):157
79. Kachanov LM (1958) Proc Acad Sci USSR Div Eng Sci 8:26
80. Chaboche JL (1984) Nucl Eng Des 79(3):309
81. Lemaitre J (1986) Eng Fract Mech 25(5-6):523
82. Lemaitre J, Desmorat R (2005) Engineering Damage Mechanics: Ductile, Creep, Fatigue and Brittle Failures. Springer, Berlin
83. Tai WH, Yang BX (1986) Eng Fract Mech 25(3):377
84. Tai WH (1990) Eng Fract Mech 37(4):853
85. Chandrakanth S, Pandey PC (1993) Int J Fract 60:R73
86. Bouchard PO, Bourgeon L, Fayolle S, Mocellin K (2011) Int J Mater Form 4:299
87. Saanouni K, Chaboche J (2003) Comprehensive Structural Integrity. In: Milne I, Ritchie R, Karihaloo B (eds). Pergamon, Oxford, pp 321–376
88. Cao TS, Gachet JM, Montmitonnet P, Bouchard PO (2014) Eng Fract Mech 124-125(0):80
89. Cao TS, Bobadilla C, Montmitonnet P, Bouchard PO (2013) Key Eng Mater 213:554–557
90. Malcher L, Mamiya E (2014) Int J Plast 56(0):232
91. Cao TS, Bobadilla C, Montmitonnet P, Bouchard PO (2015) J Mater Process Technol 216(0):385
92. Gologanu M, Leblond JB, Devaux J (1994) J Mater Process Technol 116(3):290
93. Kao AS, Kuhn HA, Richmond O, Spitzig WA (1990) J Mater Res 5(1):83
94. Cao TS, Maire E, Verdu C, Bobadilla C, Lasne P, Montmitonnet P, Bouchard PO (2014) Comput Mater Sci 84(0):175
95. Bouaziz O, Maire E, Giton M, Lamarre J, Salingue Y, Dimichiele M (2008) Revue de Métallurgie 105:102
96. Koplik J, Needleman A (1988) Int J Solids Struct 24(8):835
97. Xia L, Cheng L (1997) Int J Fract 87(3):289
98. Faleskog J, Gao X, Shih CF (1998) Int J Fract 89(4):355
99. Steglich W, Brocks W (1998) Fatigue Fract Eng Mater Struct 21(10):1175
100. Pardoen T, Doghri I, Delannay F (1998) Acta Mater 46(2):541
101. Corigliano A, Mariani S, Orsatti B (2000) Int J Fract 104(4):349
102. Kim J, Gao X, Srivatsan TS (2004) Eng Fract Mech 71(3):379
103. McElwain D, Roberts A, Wilkins A (2006) Acta Mater 54(8):1995
104. Nielsen KL, Tvergaard V (2009) Int J Solids Struct 46(3-4):587
105. Cazacu O, Revil-Baudard B, Lebensohn RA, Garajeu M (2013) J Appl Mech 80(6):064501
106. Benallal A, Desmorat R, Fournage M (2014) Eur J Mech A Solids 47(0):400
107. Leblond JB, Morin L (2014) J Appl Mech 81(5):051012
108. Madou K, Leblond JB (2012) J Mech Phys Solids 60(5):1037
109. Kailasam M, Ponte Castañeda P (1998) J Mech Phys Solids 46(3):427

110. Aravas N, Ponte Castañeda P (2004) Comput Methods Appl Mech Eng 193(36-38):3767
111. Danas K, Aravas N (2012) Homogenization and Micromechanics of Smart and Multifunctional Materials. Compos Part B 43(6):2544
112. Ponte Castañeda P (1991) J Mech Phys Solids 39(1):45
113. Ponte Castañeda P, Zaidman M (1994) J Mech Phys Solids 42(9):1459
114. Zaidman M, Ponte Castañeda P (1996) Int J Solids Struct 33(9):1287
115. Danas K, Ponte Castañeda P (2009) Eur J Mech A Solids 28(3):387
116. Danas K, Ponte Castañeda P (2009) Eur J Mech A Solids 28(3):402
117. Cao TS, Mazière M, Danas K, Besson J (2015) Int J Solids Struct 63(0):240
118. Garajeu M, Suquet P (1997) J Mech Phys Solids 45(6):873
119. Sun Y, Wang D (1989) Acta Mech Sinica 5(3):237
120. Needleman A (1972) J Appl Mech 39(4):964
121. Tvergaard V (1982) Int J Fract 18(4):237
122. Brocks W, Sun DZ, Hönig A (1995) Int J Plast 11(8):971
123. Needleman A (1987) J Appl Mech 54(3):525
124. Kuna M, Sun D (1996) Int J Fract 81(3):235
125. Barsoum I, Faleskog J (2007) Int J Solids Struct 44(17):5481
126. Tvergaard V (2011) Int J Solids Struct 48(7-8):1101
127. Zybell L, Hütter G, Linse T, Mühlich U, Kuna M (2014) Eur J Mech A Solids 45(0):8
128. Keralavarma S, Benzerga AA (2010) J Mech Phys Solids 58(6):874
129. Bridgman PW (1952) Studies in large plastic flow and fracture. Harvard University Press, Cambridge
130. Peng J, Wu PD, Huang Y, Chen XX, Lloyd DJ, Embury JD, Neale KW (2009) Int J Solids Struct 46(20):3741
131. Bao Y (2005) Eng Fract Mech 72(4):505
132. Papasidero J, Doquet V, Mohr D (2015) Int J Solids Struct 459:69–70
133. Beese AM, Luo M, Li Y, Bai Y, Wierzbicki T (2010) Eng Fract Mech 77(7):1128
134. Haltom SS, Kyriakides S, Ravi-Chandar K (2013) Int J Solids Struct 50(10):1507
135. Cao TS (2013) Modeling ductile damage for complex loading paths. Ph.D. thesis, Ecole Nationale Supérieure des Mines de Paris
136. Dunand M, Mohr D (2011) J Mech Phys Solids 59(7):1374
137. Gachet JM, Delattre G, Bouchard PO (2014) Eng Fract Mech 124-125(0):121
138. Dunand M, Mohr D (2011) Eng Fract Mech 78(17):2919
139. Luo M, Dunand M, Mohr D (2012) Int J Plast 32-33(0):36
140. Mae H, Teng X, Bai Y, Wierzbicki T (2007) Mater Sci Eng A 459(1-2):156
141. Li Y, Wierzbicki T (2010) Int J Solids Struct 47(17):2316
142. Papasidero J, Doquet V, Mohr D (2014) Exp Mech 54(2):137
143. Massé T (2010) Study and optimization of high carbon steel flat wires. Ph.D. thesis, Ecole nationale supérieure des Mines de Paris
144. Cao TS, Vachey C, Montmitonnet P, Bouchard PO (2015) J Mater Process Technol 217(0):30
145. Gachet JM, Delattre G, Bouchard PO (2015) J Mater Process Technol 216(0):260
146. Bettaieb MB, Lemoine X, Bouaziz O, Habraken AM, Duchêne L (2011) Mech Mater 43(3):139
147. Fansi J, Balan T, Lemoine X, Maire E, Landron C, Bouaziz O, Bettaieb MB, Habraken AM (2013) Mater Sci Eng A 569(0):1
148. Thuillier S, Maire E, Brunet M (2012) Mater Sci Eng A 558(0):217
149. Weck A, Wilkinson DS, Maire E, Toda H (2008) Acta Mater 56(12):2919
150. Maire E, Bouaziz O, Michiel MD, Verdu C (2008) Acta Materialia 56(18):4954
151. Landron C, Maire E, Adrien J, Bouaziz O (2011) Optical Measurements, Modeling, and Metrology. In: Conference Proceedings of the Society for Experimental Mechanics Series, vol 5. Springer, New York, pp 11–18
152. Fabrègue D, Landron C, Bouaziz O, Maire E (2013) Mater Sci Eng A 579(0):92
153. Dunand M, Mohr D (2010) Int J Solids Struct 47(9):1130
154. Bouchard PO, Gachet JM, Roux E (2011) Homogenization and Micromechanics of Smart and Multifunctional Materials. In: The 14th international Esaform conference on material forming: Esaform 2011, AIP Conference Proceedings, vol 1353, p 47
155. Tardif N, Kyriakides S (2012) Int J Solids Struct 49(25):3496
156. Jirásek M (1998) Int J Solids Struct 35(31-32):4133
157. Peerlings RHJ, Borst RD, Brekelmans WAM, Vree JHPD (1996) Int J Numer Methods Eng 39:3391
158. Abbasi M, Ketabchi M, Izadkhah H, Fatmehsaria DH, Aghbash AN (2011) Procedia Engineering 10(0):415
159. He M, Li F, Wang Z (2011) Chin J Aeronaut 24(3):378
160. Besson J, Steglich D, Brocks W (2001) Int J Solids Struct 38(46-47):8259
161. Besson J, Steglich D, Brocks W (2003) Int J Plast 19(10):1517
162. Rousselier G (1987) Nucl Eng Des 105(1):97
163. Cao TS (2014) Int J Solids Struct 51(13):2370
164. El Khaoulani R, Bouchard PO (2012) Finite Elem Anal Des 59(0):1
165. Mediavilla J, Peerlings RHJ, Geers MGD (2006) International Journal For Numerical Methods In Engineering 66(4):661
166. Mediavilla J, Peerlings RHJ, Geers MGD (2006a) Comput Struct 84(8-9):604
167. Feld-Payet S, Chiaruttini V, Feyel F (2013). In: Conference Proceedings - CFRAC 2013 Repro Fetterle, Prague, Czech Republic, p 96
168. Seabra MRR, Sustaric P, Cesar de Sa JMA, Rodic T (2013) Comput Mech 52(1):161
169. Möes N, Dolbow J, Belytschko T (1999) Int J Numer Methods Eng 46(1):131
170. Besson J (2013). In: Conference Proceedings - CFRAC 2013 Repro Fetterle, Prague, Czech Republic, p 101
171. Besson J, Cao TS, Chiaruttini V, Feld-Payet S (2015) IUTAM Symposium on Ductile Failure and Localization
172. Takuda H, Mori K, Hatta N (1999) J Mater Process Technol 95(1–3):116
173. Han HN, Kim KH (2003) J Mater Process Technol 142(1):231
174. Ozturk F, Lee D (2004) J Mater Process Technol 147(3):397
175. Liu H, Yang Y, Yu Z, Sun Z, Wang Y (2009) J Mater Process Technol 209(14):5443
176. Li Y, Luo M, Gerlach J, Wierzbicki T (2010) J Mater Process Technol 210(14):1858
177. Gouveia B, Rodrigues J, Martins P (1996) Int J Mech Sci 38(4):361
178. Gouveia B, Rodrigues J, Martins P (2000) J Mater Process Technol 101(1–3):52
179. Landre J, Pertence A, Cetlin P, Rodrigues J, Martins P (2003) Finite Elem Anal Des 39(3):175
180. Hoa V, Seo D, Lim J (2005) Theor Appl Fract Mech 44(1):58
181. Liu J, Bai Y, Xu C (2013) J Manuf Sci Eng 136(1):011010
182. Cao TS, Montmitonnet P, Bouchard PO, Bobadilla C, Vachey C (2014), vol 81, Japan, p 185
183. Saanouni K, Devalan P (2013) Damage Mechanics in Metal Forming - Application to Virtual Metal Forming. John Wiley & Sons, pp 355–492

184. Bourgeon L (2009) Etude et modélisation des mécanismes d'endommagement en forge à froid. Ph.D. thesis, Ecole nationale supérieure des Mines de Paris. In French
185. Xue L (2007) Int J Solids Struct 44(16):5163
186. McAllen PJ, Phelan P (2007) J Mater Process Technol 183(2-3):210
187. Tang KK, Li ZX, Wang J (2011) Mater Des 32(6):3299
188. Cao TS, Montmitonnet P, Bouchard PO (2013) Int J Numer Methods Eng 96(9):561
189. Reusch F, Svendsen B, Klingbeil D (2003) Eur J Mech A Solids 22(6):779
190. Madou K, Leblond JB (2012) J Mech Phys Solids 60(5):1020
191. Roux E, Bernacki M, Bouchard P (2013) Comput Mater Sci 68(0):32
192. Roux E, Shakoor M, Bernacki M, Bouchard PO (2014) Model Simul Mater Sci Eng 22(7):075001
193. Shakoor M, Bernacki M, Bouchard PO (2015) Eng Fract Mech 0. (In press)
194. Pijaudier-Cabot G, Bazant ZP, Tabbara M (1988) Eng Comput 5(2):141
195. Forest S, Sievert R (2006) Int J Solids Struct 43(24):7224
196. Forest S (2009) J Eng Mech 135(3):117
197. Niazi M, Wisselink H, Meinders T (2013) Comput Mech 51(2):203
198. Jirásek M (1998) Int J Solids Struct 35(4133):31–32
199. Bažant Z, Jirásek M (2002) J Eng Mech 128(11):1119
200. Eringen A, Suhubi E (1964) Int J Eng Sci 2(2):189
201. Suhubl E, Eringen A (1964) Int J Eng Sci 2(4):389
202. Bargellini R, Besson J, Lorentz E, Michel-Ponnelle S (2009). In: Proceedings of the 17th International Workshop on Computational Mechanics of Materials IWCMM-17, vol 45, p 762
203. Needleman A (1988) Comput Methods Appl Mech Eng 67(1):69
204. D. J. P. C. G. B C (1996) J Eng Mech 122(10):939
205. Sluys L, Borst de R (1992) Int J Solids Struct 29(23):2945
206. Bazant ZP, Pijaudier-Cabot G (1988) J Appl Mech 55
207. Aifantis EC (1992) Int J Eng Sci 30(10):1279
208. Erice B, Gálvez F, Cendón D, Sánchez-Gálvez V (2012) Eng Fract Mech 79(0):1
209. Khan AS, Liu H (2012) Int J Plast 37(0):1
210. Roth CC, Mohr D (2014) Int J Plast 56(0):19
211. Krajcinovic D, Fonseka GU (1981) J Appl Mech 48(4):809
212. Chow C, Wang J (1987) Eng Fract Mech 27(5):547
213. Chow C, Wang J (1988) Eng Fract Mech 30(5):547
214. Chow C, Wang J (1988) Int J Fract 38(2):83
215. Chow C, Lu T (1989) Eng Fract Mech 34(3):679
216. Steinmann P, Carol I (1998) Int J Eng Sci 36(15):1793
217. Lemaitre J, Desmorat R, Sauzay M (2000) Eur J Mech A Solids 19(2):187
218. Chaboche JL (1981) Nucl Eng Des 64(2):233
219. Krajcinovic D (1985) J Appl Mech 52(4):829
220. Lubarda V, Krajcinovic D (1993) Int J Solids Struct 30(20): 2859
221. Monchiet V, Cazacu O, Charkaluk E, Kondo D (2008) Int J Plast 24(7):1158
222. Keralavarma SM, Benzerga AA (2008) Comptes Rendus Mécanique 336(9):685
223. Hill R (1948). In: Proceedings of the Royal Society of London, vol 193, p 281
224. Barlat F, Yoon JW, Cazacu O (2007) Int J Plast 23(5):876
225. Bron F, Besson J (2004) Int J Plast 20(937):4–5
226. Lodej B, Niang K, Montmitonnet P, Aubin JL (2006) J Mater Process Technol 177(188):1–3
227. Bao Y, Treitler R (2004) Mater Sci Eng A 384(385): 1–2
228. Bao Y, Wierzbicki T (2005) Eng Fract Mech 72(7):1049
229. Massé T, Chastel Y, Montmitonnet P, Bobadilla C, Persem N, Foissey S (2012) Int J Mater Form 5(2):129
230. Brùnig M, Chyra O, Albrecht D, Driemeier L, Alves M (2008) Int J Plast 24(10):1731
231. Feld-Payet S, Besson J, Feyel F (2011) Int J Damage Mech 20(5):655
232. Needleman A, Tvergaard V, Van Der Giessen E (1995) Int J Damage Mech 4(2):134
233. Tvergaard V (2008) Int J Mech Sci 50(10–11):1459
234. Tvergaard V (2009) Int J Fract 158(1):41
235. Nielsen K, Dahl J, Tvergaard V (2012) Int J Fract 177(2):97